



UNIVERSITÀ
DEGLI STUDI
DI PADOVA



DIPARTIMENTO
DI INGEGNERIA
DELL'INFORMAZIONE

Università degli Studi di Padova

DEPARTMENT OF INFORMATION ENGINEERING

Master's Degree in Bioengineering

Comparative analysis of TMS-EEG signal using different approaches in healthy subjects

Supervisor

Prof.ssa Alessandra Bertoldo

Candidate

Matteo Panizzolo Terrin

Co-Supervisors

Prof. Camillo Porcaro

Prof.ssa Florinda Ferreri

Academic year 2022 – 2023

October 26th 2023

*“Lo duca e io per quel cammino ascoso
intrammo a ritornar nel chiaro mondo;
e senza cura aver d’alcun riposo,*

*salimmo sù, el primo e io secondo,
tanto ch’i’ vidi de le cose belle
che porta ’l ciel, per un pertugio tondo.*

E quindi uscimmo a riveder le stelle.”

Abstract

The integration of transcranial magnetic stimulation with electroencephalography (TMS-EEG) represents a useful non-invasive approach to assess cortical excitability, plasticity and intra-cortical connectivity in humans in physiological and pathological conditions.

However, biological and environmental noise sources can contaminate the TMS-evoked potentials (TEPs). Therefore, signal preprocessing represents a fundamental step in the analysis of these potentials and is critical to remove artefactual components while preserving the physiological brain activity.

The objective of the present study is to evaluate the effects of different signal processing pipelines, (namely Leodori et al., Rogasch et al., Mutanen et al.) applied on TEPs recorded in five healthy volunteers after TMS stimulation of the primary motor cortex (M1) of the dominant hemisphere. These pipelines were used and compared to remove artifacts and improve the quality of the recorded signals, laying the foundation for subsequent analyses. Various algorithms, such as Independent Component Analysis (ICA), SOUND, and SSP-SIR, were used in each pipeline.

Furthermore, after signal preprocessing, current localization was performed to map the TMS-induced neural activation in the cortex. This methodology provided valuable information on the spatial distribution of activity and further validated the effectiveness of the signal cleaning pipelines.

Comparing the effects of the different pipelines on the same dataset, we observed considerable variability in how the pipelines affect various signal characteristics. We observed significant differences in the effects on signal amplitude and in the identification and characterisation of peaks of interest, i.e., P30, N45, P60, N100, P180. The identification and characteristics of these peaks showed variability, especially with regard to the early peaks, which reflect the cortical excitability of the stimulated area and are the more affected by biological and stimulation-related artifacts.

Despite these differences, the topographies and source localisation, which are the most informative and useful in reconstructing signal dynamics, were consistent and reliable between the different pipelines considered.

The results suggest that the existing methodologies for analysing TEPs produce different effects on the data, but are all capable of reproducing the dynamics of the signal and its components. Future studies evaluating different signal preprocessing methods in larger populations are needed to determine an appropriate workflow that can be shared through the scientific community, in order to make the results obtained in different centres comparable.

Sommario

L'integrazione della stimolazione magnetica transcranica con l'elettroencefalogramma (TMS-EEG) rappresenta un approccio non invasivo nella valutazione dell'eccitabilità e della plasticità corticale e della connettività intra-corticale nell'uomo in condizioni fisiologiche e patologiche. Tuttavia, le fonti di rumore biologico e ambientale possono determinare una contaminazione dei potenziali evocati dalla TMS (TEP). Pertanto, la pre-elaborazione del segnale rappresenta un passo fondamentale nell'analisi di questi potenziali ed è fondamentale per rimuovere le componenti artefattuali preservando l'attività cerebrale fisiologica.

L'obiettivo del presente studio è valutare gli effetti di diverse *pipeline* di elaborazione del segnale (Leodori et al., Rogasch et al. e Mutanen et al.) applicate ai TEP registrati in cinque volontari sani dopo stimolazione TMS della corteccia motoria primaria (M1) dell'emisfero dominante. Queste *pipeline* sono state utilizzate e confrontate per rimuovere gli artefatti e migliorare la qualità dei segnali registrati, ponendo le basi per le analisi successive. In ogni *pipeline* sono stati utilizzati diversi algoritmi di processamento del segnale, come l'analisi delle componenti indipendenti (ICA), SOUND e SSP-SIR. Inoltre, dopo la pre-elaborazione del segnale, è stata eseguita la localizzazione di corrente per localizzare l'attivazione neurale indotta dalla TMS nella corteccia. Questa metodologia ha fornito informazioni sulla distribuzione spaziale dell'attività e ha ulteriormente convalidato l'efficacia delle *pipeline*.

Confrontando i risultati delle diverse pipeline, abbiamo osservato come le varie caratteristiche del segnale vengano influenzate in modo variabile da quest'ultime. Sono state osservate differenze significative nell'ampiezza del segnale processato e nell'identificazione e caratterizzazione dei picchi di attività di interesse, ossia P30, N45, P60, N100 e P180. L'identificazione e le caratteristiche di questi picchi hanno mostrato un certo grado di variabilità, in particolare nei picchi precoci, che riflettono l'eccitabilità corticale dell'area stimolata e sono i più influenzati da numerosi artefatti associati alla stimolazione e biologici. Nonostante queste differenze, le topografie e la localizzazione della sorgente, che sono le più informative e utili per ricostruire la dinamica del segnale, sono coerenti e affidabili tra le diverse pipeline considerate.

I risultati suggeriscono che le metodologie esistenti per l'analisi dei TEP producono effetti diversi sui dati, ma sono tutte in grado di riprodurre la dinamica del segnale e delle sue componenti. Sono necessari studi futuri che valutino diversi metodi di elaborazione del segnale in popolazioni più ampie per determinare un metodo di elaborazione appropriato che possa essere condiviso dalla comunità scientifica, al fine di rendere confrontabili i risultati ottenuti in diversi centri.

Contents

Introduction	1
1.1 Transcranial Magnetic Stimulation	2
1.2 Electroencephalography	4
1.3 TMS-EEG	6
1.4 Transcranial Evoked Potentials	7
1.5 The artifact problem	9
1.6 Algorithms	13
1.7 Source Localization	23
Materials and Methods	29
2.1 Subjects.....	29
2.2 Instrumentation.....	30
2.3 Experimental Protocol	31
2.4 Data processing	32
2.6 Toolboxes.....	38
2.7 Data analysis.....	40
Results	43
3.1 Group analysis	43
3.2 Individual analysis.....	50
Discussion.....	61
Conclusions	65
References	67

Introduction

During the past decade, the combined use of transcranial magnetic stimulation (TMS) and electroencephalography (EEG) has gained popularity as a valuable method for studying cortical excitability and connectivity [1]. TMS-evoked potentials (TEPs), which are cortical responses synchronized with the TMS pulse, offer insights into cortical excitability and effective connectivity within the stimulated brain area and the activated networks [2]–[4]. TEPs provide information on the state of the stimulated cortical region and its functional relationships with connected areas, without relying on a priori assumptions as required by functional magnetic resonance imaging (fMRI) or EEG alone [1]. Consequently, TEPs are employed in clinical research to investigate neurophysiological alterations associated with several psychiatric and neurological disorders [5]. For instance, TEPs have been used to distinguish between different clinical subtypes of patients with disorders of consciousness [6] and as a marker of disease progression in Alzheimer's disease [7]. Therefore, TEPs have been proposed as biomarkers for enhancing diagnosis and monitoring treatment-induced neurophysiological changes [1].

It is crucial to demonstrate high reliability to develop a useful biomarker, which is often equated with reproducibility [1]. Reliability refers to the extent to which a measurement is free from variable errors [1], [8], enabling the reliable detection of meaningful signal changes. Assessing reliability involves conducting the same measurement using different instruments (internal consistency), different raters (inter-rater reliability), or the same rater over time (intra-rater reliability or test-retest reliability) [1], [8], [9]. While some studies have evaluated the test-retest reliability of TEPs and found overall high reliability for different TEP components, particularly at later latencies [10]–[13], these assessments were performed using the same pipeline for data analysis [1]. However, the reproducibility of TEPs analysis may be influenced by the heavy contamination of these signals by TMS-related stimulation artifacts, which can be significantly larger in magnitude than the EEG signal and time-locked to the TMS pulse, consequently reducing the signal-to-noise ratio (SNR)[1]. Furthermore, several biological (i.e., cardiac activity, eye and jaw movements) and non-biological (i.e., power line, electrodes displacement and noise during the recordings) may contaminate TEPs recordings.

To address this issue, various methodologies and algorithms have been developed to remove artifacts while preserving physiological brain signals [1], [14].

The preprocessing phase enables the extraction of TEPs, but it can also impact their reproducibility [1]. Among the most used algorithms we can find the Independent Component Analysis (ICA), the Source-Estimate-Utilizing Noise-Discarding (SOUND) algorithm, the Signal-Space Projection (SSP) and the Source-Informed Reconstruction (SIR).

Specifically, the use of different artifact reduction approaches by different users may affect the inter-rater reliability of TEPs. Furthermore, the test-retest reliability can vary across studies due to the use of different approaches [1].

The objective of this study is to assess the amount of variability introduced in TEPs by employing different preprocessing pipelines. To achieve this, we processed the same TMS-EEG datasets using three pipelines that we named: Leodori et.al [15], Rogash et. al [16], and Mutanen et. al [17], [18], and compared the resulting TEPs. Although these pipelines share the common goal of removing artifacts while preserving the neuronal signal in TMS-EEG recordings, they employ different strategies. Leodori et.al and Rogasch utilize two stages of ICA as a core function for isolating and removing artifacts. Mutanen et. al employs ICA solely for removing ocular artifacts, with its core functions being the SOUND [17] and the SSP-SIR [18]. These differences in processing methods may influence the amplitude and topography of TEP components, ultimately affecting their reproducibility.

1.1 Transcranial Magnetic Stimulation

TMS is a well-established neuromodulation technique involving the application of a strong and brief magnetic field pulses over the scalp, able to produce neuronal activation in underlying cortical areas. TMS relies on electromagnetic induction, which is described by Faraday's law [19]. It involves passing an intense current through a dedicated coil to produce a time-varying magnetic field that penetrates the scalp and the skull. The changing magnetic field induces an electric field in the cortex, which can depolarize neurons in the stimulated area. The stimulation involves axons rather than cell bodies of neurons, since the latter have a much longer electrical time constant and higher threshold [20]. Axonal depolarization can trigger action potentials that travel along the axons orthodromically towards their terminal and antidromically to the cell body [19], [21]. As the excited axons impinge on other neurons, it causes trans-synaptic activation and the generation of post-synaptic currents in the dendritic

arboreal of cortical pyramidal neurons at the target site. These currents can be spatially and temporally summed, and if the summation is significant enough and involves a large area of the cortex, it leads to a measurable EEG signal [19]. Additionally, the activation of pyramidal neurons can also result in secondary excitation or inhibition of connected subcortical structures and cortical regions. When the stimulation intensity is appropriate, locally evoked action potentials can propagate across cortical layers and different brain regions, leading to the activation of an entire network. Therefore, TMS might not only stimulate the target area but also indirectly activate interconnected regions, which is advantageous for brain connectivity studies [19]. The summation of postsynaptic currents in the dendritic arbour of connected cortical areas can contribute to a measurable EEG signal, which contributes to the transcranial evoked EEG response [19].

The magnetic pulse in TMS is of the order of 1-3 T with a rise time of approximately 50-100 ms. Due to its short pulse duration, TMS has sub-millisecond temporal resolution, allowing for real-time modulation of brain activity [19]. The extent of cortical area stimulated by TMS depends on factors such as coil geometry, stimulus intensity, target area, and the distance between the coil and the cortex. Several coil designs can be used for TMS stimulation, such as circular, butterfly-shaped and figure-of-eight coils. Because of the higher focality of the stimulation, figure-of-eight coils are usually preferred to target specific cortical regions. These coils consist of two overlapping small round coils with oppositely directed currents, with the highest stimulation intensity at the intersection of the coil windings [19], [22].

Concerning stimulation intensity, magnetic fields attenuate rapidly with distance, and the stimulation is strongest in superficial cortical layers compared to deeper layers. However, the induced neuronal activity also depends on other factors such as the position, orientation, and membrane characteristics of the neuronal structures. The cascade of events accompanying TMS is illustrated in Figure 3 [19].

When applied alone, TMS allows the study of the excitability and plasticity of the stimulated cortex. Most TMS studies have been performed by targeting the primary motor cortex (M1) because its stimulation, unlike other cortical areas, can produce a measurable peripheral signal known as Motor Evoked Potential (MEP). In fact, by activating the cortico-spinal tract originating from the descending axons of M1 pyramidal cells, TMS pulses produce a muscular activation that can be recorded by EMG. Therefore, by measuring MEPs characteristics (i.e., amplitude and latency) it is possible to evaluate indirectly the neurophysiological characteristics of M1.

However, the brain activity evoked by TMS can be measured more directly by using various techniques such as EEG, fMRI, near-infrared spectroscopy, and positron emission tomography. Among these, EEG has been the most successful and commonly used in combination with TMS. This is due to its high temporal resolution, wide availability, lower cost compared to other techniques, and technical compatibility for online integration with TMS [19].

1.2 Electroencephalography

The electroencephalogram (EEG) is a real-time, non-invasive neurophysiological technique for recording the brain's electrical activity by placing electrodes on the scalp. The first EEG recording was conducted by Hans Berger, a German psychiatrist, in 1924 [23]. EEG devices measure the potential differences between scalp electrodes, which reflect localized depolarizations and hyperpolarisations of post-synaptic neurons, known as excitatory postsynaptic potentials (EPSP) and inhibitory postsynaptic potentials (IPSP), respectively[23].

The voltage variances can be assessed in two ways: either by comparing the readings between pairs of scalp electrodes (referred to as bipolar) or by contrasting the measurements between individual electrodes and a common reference point (known as unipolar). In the latter arrangement, the reference point is typically an inactive site on the scalp [23]. The amplitude of EEG signals for healthy individuals is around 100 μ V, and the bandwidth ranges from under 1 Hz to approximately 80 Hz. Different frequency bands, such as alpha (α), beta (β), delta (δ), theta (θ), and gamma (γ) waves, can be distinguished from the EEG signal based on their frequency spectrum. Brain signals with higher frequencies (80-500 Hz) have also been described, however their physiological and pathological significance is still under investigation.

EEG recordings offer high temporal resolution due to their sampling rate, which usually ranges between 250 and 5000 Hz. The location of electrodes on the scalp follows the international 10-20 system, which uses measurements from four standard positions on the head (nasion, inion, right and left preauricular points) to determine the positions of 21 electrodes [23]. However, the spatial resolution with the standard electrode configurations used in clinical setting (low-density EEG) is limited. To overcome this issue, a higher number or electrodes can be placed to increase the topographical accuracy of the technique. High-

density electrode configurations can involve up to 320 electrodes and employ the 10-10 or 10-5 placement systems [23]. Even with high-density recording the precise locations and extent of brain activation can only be identified using sophisticated spatial filtering and interpolation methods must be applied.

EEG signals can be affected by various types of biological, instrumental, or environmental noise and artifacts. Bioelectric artifacts can arise from movements (particularly eye and jaw movements, which can interfere with EEG recordings due to their proximity to the scalp), heartbeat, sweating, and breathing [23]. Artifacts are typically identified by their temporal relationship to other bioelectrical signals, such as electrocardiogram (ECG), electrooculogram (EOG), or electromyogram (EMG), their typical morphology, or difficulties in interpreting their electrical field in a biologically plausible manner [23].

Furthermore, scalp EEG electrodes predominantly capture activity correlated over large areas of the superficial layers of the cerebral cortex as illustrate in figure, with smaller contributions from deeper structures [23].

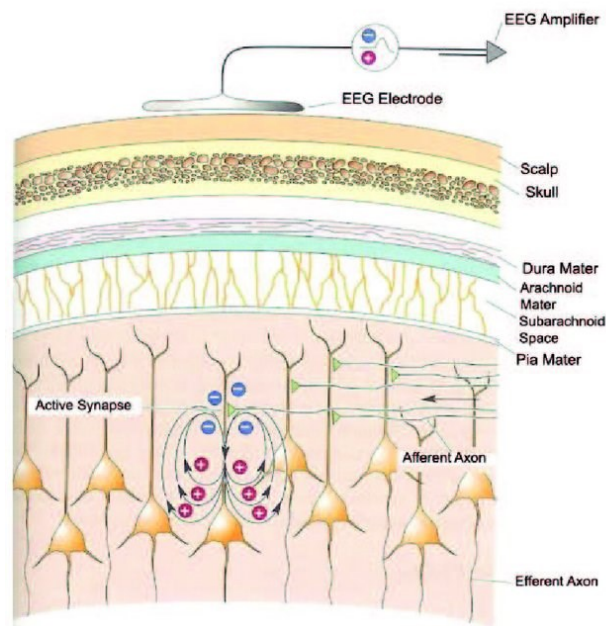


Figure 1: EEG principle: electrical fields generated by aligned pyramidal cell [24].

Alternative approaches to acquire brain activity, based on the same principles of EEG are represented by Electrocorticography (ECoG) and intracranial electroencephalography (iEEG). These methods enable the measurement of bioelectric events generated by individual neurons using invasive microelectrodes targeting specific cells of interest [23]. The magnitude of signals captured directly from the brain's surface using invasive microelectrodes typically falls within the range of 1 to 2 millivolts (mV) [23].

	Frequency band	Characteristic stage	Location
Delta	0.5-4 Hz	Deep sleep	Deep structures
Theta	4-8 Hz	Relaxation, drowsiness, sleep	Frontal regions
Alpha	8-14 Hz	Relaxation, thinking, closed-eyes	Occipital regions
Beta	14-30 Hz	Active thinking, focus, high alert	Parietal and frontal lobes
Gamma	>30 Hz	Combination of sensory processing	Somatosensory cortex

Table 1: EEG characteristic waves: In the EEG signals, it is possible to differentiate five different waves according to different frequency band [23].

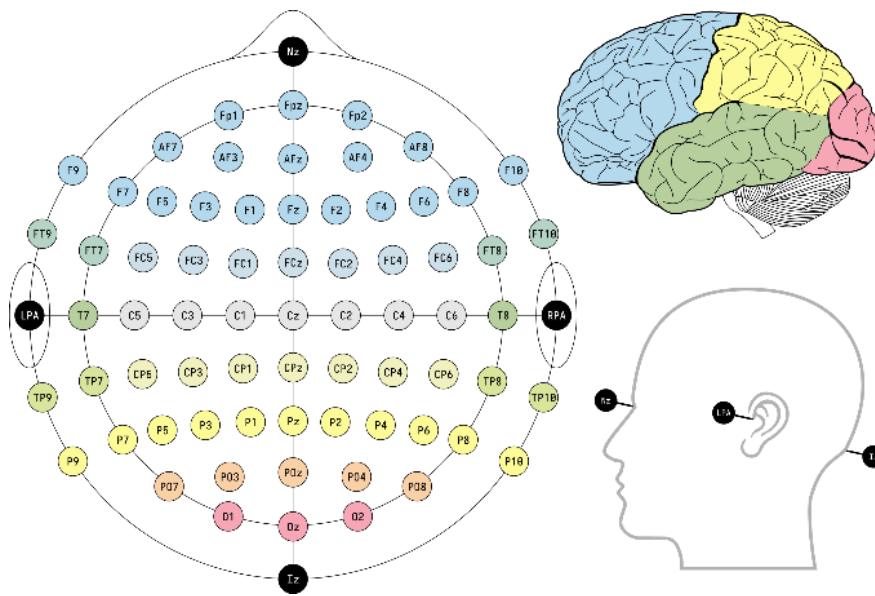


Figure 2: 10-10 system for electrodes placement. The colours of the electrodes and the labels (F, C, P, O, and T) are in accordance with the corresponding brain lobes [25].

In clinical settings, EEG recordings are utilized to examine the brain's spontaneous electrical activity over a period of time, investigate event-related potentials, analyse spectral content, and diagnose conditions such as epilepsy, sleep disorders, anaesthesia depth, strokes, coma, encephalopathies, and brain death [23].

1.3 TMS-EEG

The integration of TMS with EEG has been valuable in approaching fundamental questions in neuroscience from novel perspectives [19]. These two techniques complement each other effectively. TMS provides causal information, overcoming the correlational nature of EEG data, while EEG allows for the recording of brain activity across the entire scalp, providing a comprehensive view of the electrical field (E-field) generated by TMS [19]. The combination

of TMS and EEG offers the advantage of using outcome measures derived from EEG responses to TMS, such as evoked potentials or brain oscillations, as neurophysiological markers of excitability or connectivity in any brain area [19]. This includes regions where TMS alone does not produce observable indicators of cortical or corticospinal excitability, such as MEPs or phosphenes. While TMS-EEG data can be analysed in both the time and frequency domains, most studies have primarily focused on the former, examining the TMS-evoked potentials (TEPs) [19].

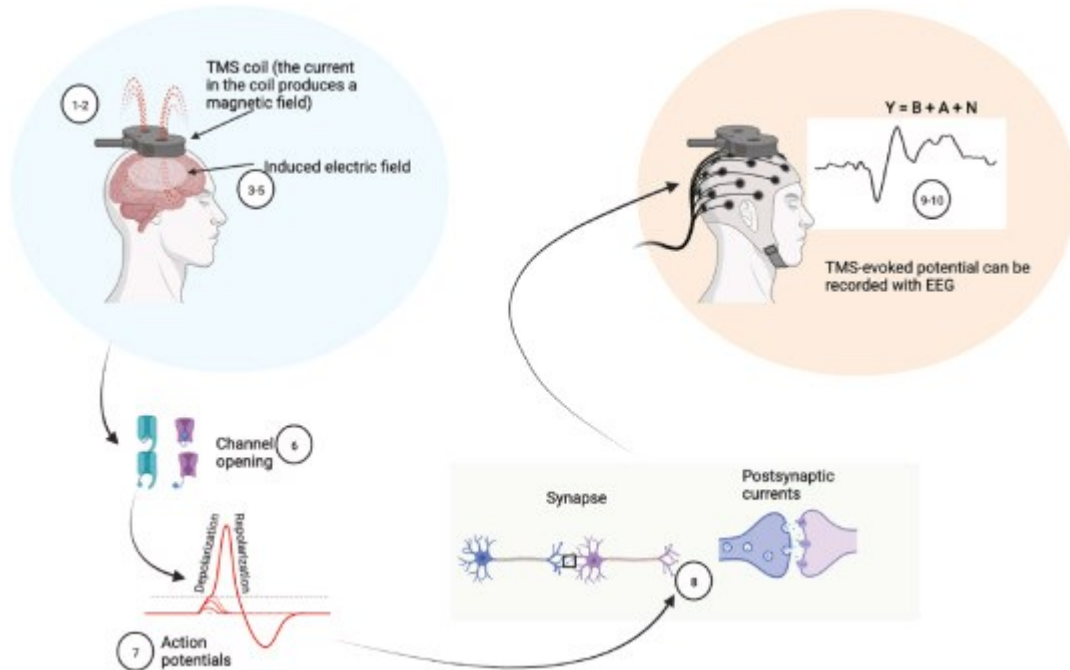


Figure 3: Chain of events triggered by the TMS pulse [19].

1.4 Transcranial Evoked Potentials

TEPs (TMS-evoked potentials) are brain potentials that occur in response to the TMS pulse, time-locked with the magnetic stimulus [19]. To study TEPs, the signal is averaged across multiple trials. The initial response to TMS is believed to be generated by the activation of neurons in the targeted area, followed by the activation of interconnected areas through axonal pathways. TEPs consist of positive (P) and negative (N) deflections that represent a combination of excitatory and inhibitory postsynaptic potentials, like event-related potentials (ERPs) [19]. While the neurophysiological mechanisms underlying TEPs are not fully understood, they are considered a reliable measure of cortical reactivity. TMS applied to the M1 elicits several peaks in the TEP waveform, occurring at approximately 15 (N15), 30

(P30), 45 (N45), 60 (P60), 100 (N100), and 180 (P180) milliseconds [19]. However, recent findings suggest that later peaks beyond 80 ms, such as N100 and P180, may be influenced by sensory-evoked responses (i.e., auditory and tactile stimulation), while very early peaks like N15 can be affected by muscle responses in the cranial region [19]. TEPs can be observed within a time window of 400-500 ms around the stimulation site and in interconnected brain areas. The amplitude of certain TEP components is maximal in electrodes near the stimulation site, while others may be more prominent in distant electrodes, such as those on the contralateral hemisphere. TEP characteristics and time courses depend on factors such as the stimulated area, coil orientation, and functional state of the underlying cortex, which can be influenced by behaviour, level of consciousness, and neuropsychiatric conditions [19]. Additionally, TEP amplitudes are affected by the stimulation intensity of the TMS pulse. TMS effects on brain activity can also be explored in the frequency domain. When a cortical area is perturbed by TMS, the neuronal response measured by EEG tends to oscillate at a specific natural frequency. This response may be attributed to the synchronization of ongoing local brain oscillations by the TMS pulse's impact on the targeted cortex. TMS-EEG allows for the manipulation and investigation of brain rhythms by assessing the impact of TMS on EEG signals and associated behavioural effects [19]. The same methods used for studying EEG oscillations can be applied to TMS-triggered oscillations. However, it is important to distinguish between TMS-evoked responses (phase-locked signals that survive averaging) and TMS-induced responses (non-phase-locked signals that cancel out during averaging). The latter requires the calculation of time-frequency representations at the single-trial level, followed by averaging to preserve the oscillatory activity that is related to but not phase-locked to the TMS pulse [19]. This measure, sometimes referred to as TMS-related spectral perturbation (TRSP) or time-frequency representations (TFR), reveals a mixture of phase-locked and non-phase-locked responses that are challenging to disentangle [19]. Throughout this thesis, the term TEPs is predominantly used to describe EEG responses to TMS, but the same considerations apply to TMS-evoked and TMS-induced oscillatory activity, unless otherwise specified.

1.5 The artifact problem

The application of TMS can produce various types of artifacts, categorized as non-physiological or physiological in nature. These artifacts may occur in relation to the timing of the TMS pulse or independently of it [19]. Numerous studies [2], [16], [26]–[28] have documented and discussed these artifacts [19]. In this section, we will examine the main EEG artifacts associated with TMS.

1.5.1 Non-physiological artifacts

1.5.1.1 Pulse artifact

The most significant artifact generated by the TMS pulse is the largest in size (Fig. 4). This artifact is electromagnetic in nature and is generated by the electromotive force induced in the loops created by the EEG electrode leads. Its amplitude can reach several Volts and saturates the EEG amplifiers obscuring brain signals. As a result, it limits the recording of EEG signals during the delivery of the TMS pulse [19].

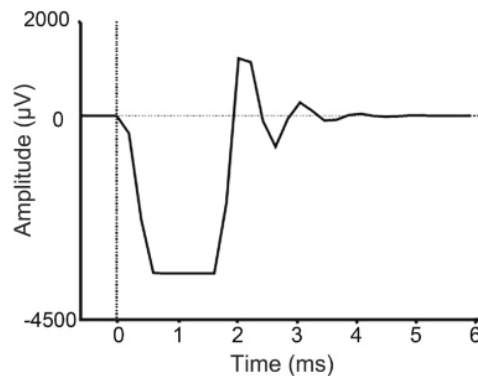


Figure 4: TMS pulse artifact recorded using a sampling rate of 5 kHz and an anti-aliasing low-pass filter of 1 kHz; signal saturation can be seen for the first large negative deflection at about 1 ms [19].

1.5.1.2 Decay artifact

Different terms such as decay artifact, discharge artifact, or electrode polarization artifact have been used by various authors to describe this phenomenon [2], [16], [19], [28], [29]. The artifact occurs when electric currents between the electrolyte gel and the recording EEG electrode polarize the electrode-skin interface. When an electrode becomes polarized, it takes a significant amount of time, often hundreds of milliseconds after the TMS pulse, for the charges to return to equilibrium [19]. During this process, an exponentially decaying charge is observed, with the decay rate being proportional to the remaining polarization voltage [19], [30]. It is important to note that this artifact can consist of multiple decaying components, each with its own characteristic time constants [19].

1.5.1.3 Electrode motion artifacts

This artifact, which is commonly observed [31], originates from mechanical factors. It occurs due to the movement of the electrode against the electrolyte gel and the gel against the skin. [19] There are several possible causes for this artifact: a) it can result from the vibration of the TMS coil, which is transmitted to the electrodes through direct contact, as well as the repelling magnetic force caused by the electric current induced in the electrode and wires by the magnetic pulse [19], [32], [33]; b) muscle twitches or head movements induced by the TMS pulse; c) contact between the coil or operator and the electrodes; d) skin stretching caused by movement, leading to shifts in skin potential [34], [19].

Motion artifacts, whether directly (a) or indirectly (b) induced by the pulse delivery, typically occur within the first ~10 ms after the TMS pulse [19]. However, they are often masked by the pulse artifact, the cranial muscle response, and the decay artifact. In some cases, artifacts resulting from skin stretching due to cranial muscle contractions can persist for longer periods [19], [34]. Additionally, as relatively recently reported [35], artifacts can occur simply due to the contact between the TMS coil and EEG electrodes, affecting both pre- and post-pulse EEG activity [19].

1.5.1.4 Power line artifact

The power line artifact, also known as the power line interference, is a common artifact observed in EEG analysis. It is caused by the electrical power system's frequency and its harmonics, which can contaminate the EEG signal.

The standard power supply frequency varies across countries, with 50 Hz in most parts of Europe and 60 Hz in North America. In EEG recordings, the power line artifact appears as a regular sinusoidal waveform at the powerline frequency (e.g., 50 Hz or 60 Hz). This artifact can interfere with the analysis and interpretation of EEG signals, making it essential to identify and minimize its effects [16].

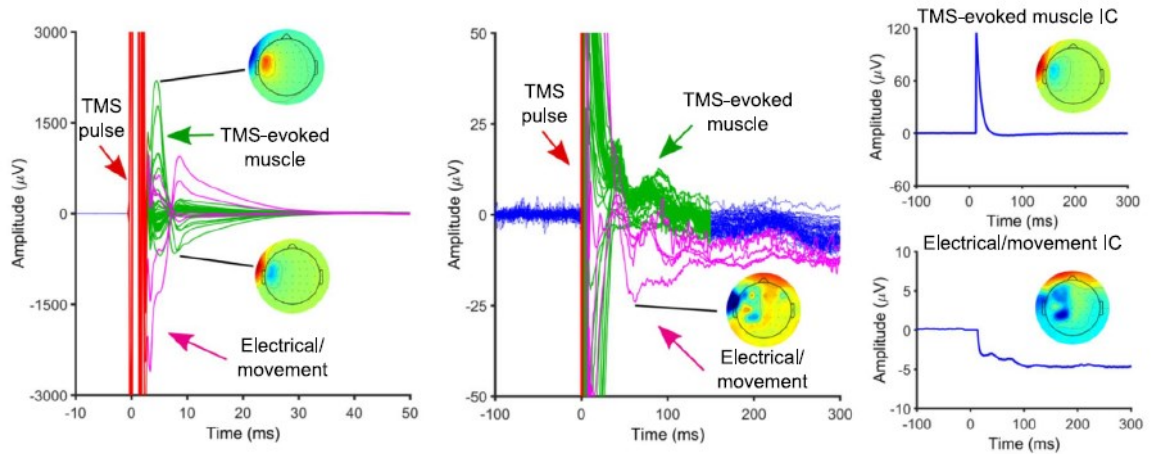


Figure 5: Artifacts in electroencephalographic (EEG) signals consequential from single transcranial magnetic stimulation (TMS) pulses [16].

1.5.2 Physiological artifacts

1.5.2.1 Eye blinks and eye movements artifacts

Eye blink artifacts are frequently observed in conventional EEG recordings and occur spontaneously [19]. These artifacts are a result of a strong dipole, with positive and negative poles located at the front and back of the eye, respectively. This dipole generates a stable and prominent electrical field potential that extends to the surrounding areas of the head, gradually diminishing towards the back of the head [19], [36], [37]. Eye movements cause slight variations in the dipole, leading to significant deflections in the EEG signal. In the context of TMS, ocular artifacts can be induced as part of a startle reflex triggered by the sound of the TMS coil click [19].

1.5.2.2 Cranial muscle artifact

These artifacts are produced by the TMS pulse when the muscles innervating the head/face are stimulated, resulting in significant contamination of the EEG signal [19]. It is important to note that these artifacts are time-locked responses and should not be confused with the muscle artifacts typically observed in EEG-only recordings, which stem from tonic muscle activity or spontaneous movements [19]. The muscle artifacts evoked by TMS are often biphasic deflections and can be up to three orders of magnitude stronger (measured in millivolts) than the neuronal responses (measured in microvolts). Their duration varies depending on the activated muscle, typically lasting around 10 to 30 milliseconds, followed by a slow return to baseline. These muscle artifacts peak within milliseconds after the TMS pulse delivery, significantly impacting the early responses to TMS [19], [38], [39].

The origin of these artifacts can be attributed to the depolarization of intramuscular motor nerve endings or the activation of cranial motor nerves, like the facial trigeminal nerves [19], [40]. As a result, they represent multiple muscle action potentials, like those observed when TMS is applied to the median nerve and evokes muscle responses in the hand. The muscles most likely to be activated depend on the placement of the TMS coil and commonly include the neck, facial muscles [41], frontal muscles, temporal muscles, or masseter muscle [19]. The proximity of the TMS target to lateral aspects of the head, language areas such as Broca's and Wernicke's areas, and the dorsolateral prefrontal cortex can elicit large muscle artifacts due to the activation of specific muscle groups [19], [38], [39], [42], [43].

It is important to note that cranial muscle contractions can cause electrode movements and stretch the skin above them. This can result in disturbances in the electrode-electrolyte-skin interfaces and electrode motion artifacts. As a consequence, the topography of decay artifacts (previously mentioned) and muscle artifacts often exhibit a correlation, particularly with larger and longer decay artifacts observed for electrodes positioned over cranial muscles [19].

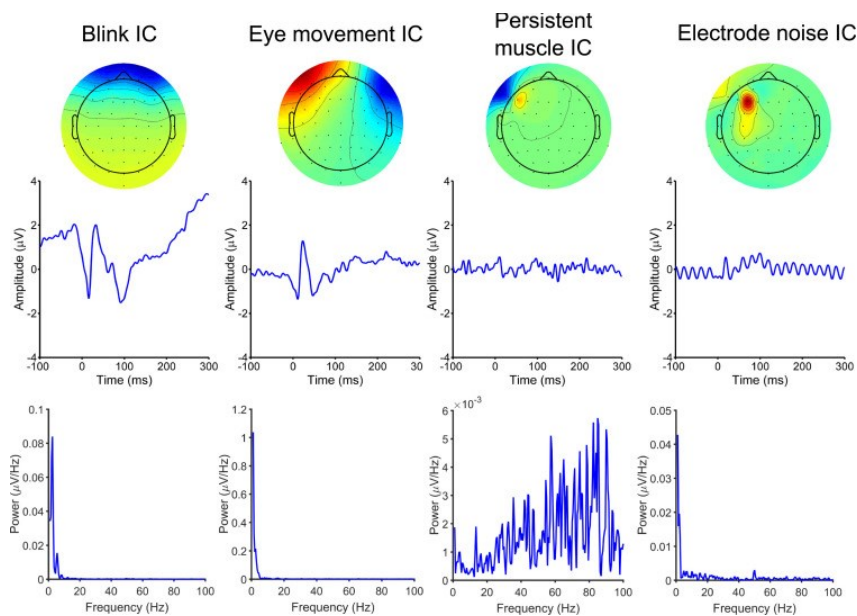


Figure 6: Other typical electroencephalographic (EEG) artifacts detected in concurrent transcranial magnetic stimulation (TMS) recordings [16].

1.5.3 Online and offline approaches for reducing artifacts in TMS-EEG data

Artifacts in TMS-EEG signals have prompted the development of various approaches to minimize their impact [14]. These methods can be broadly categorized into online and offline approaches. Online approaches aim to avoid artifacts during data collection, employing

techniques such as using robust equipment, careful electrode-skin preparation, delaying TMS device capacitor recharge, stimulating specific cortical regions, and using noise-masking techniques. The advantage of online methods lies in excellent signal-to-noise ratios and simplified offline cleaning. However, their suitability is limited to certain experimental designs and setups [14].

In contrast, the offline approach focuses on removing or suppressing artifacts after data collection using specialized EEG analysis methods. Blind source separation (BSS) algorithms like independent component analysis (ICA) and principal component analysis (PCA) have been modified to target TMS-evoked muscle artifacts. Source-based spatial filtering methods, such as signal-space projection (SSP) and SSP with source-informed reconstruction (SSP-SIR), have also been used [14]. Several techniques address decay artifacts, such as iterative Wiener estimation and model-based subtraction. ICA is commonly employed to suppress other common artifacts like eye blinks/movement and muscle activity. Additionally, offline methods have been tested to separate TMS-evoked sensory activity from cortical circuit activity resulting from transcranial stimulation [14].

The main benefit of the offline approach is the flexibility to target various stimulation locations. However, it comes with challenges. Many novel analysis methods for cleaning TMS-EEG data are developed in-house, limiting reproducibility for most users. The wide array of analysis approaches results in numerous cleaning pipeline combinations. Validating these methods is difficult, as the true signal of interest (TMS-evoked neural response) is unknown. Combining multiple preprocessing steps may lead to undesired interactions on the cleaned signal, making it challenging to control the outcomes [14].

1.6 Algorithms

Several existing algorithms provide means to facilitate the preprocessing of EEG spontaneous and evoked activity, including TEPs. In the next paragraphs, some of these methods will be presented more in detail: Independent Component Analysis (ICA), SOUND and SSP-SIR.

1.6.1 Independent Component Analysis (ICA)

The challenge within blind source separation (BSS) involves the identification of a matrix W that enables a linear transformation, facilitating the retrieval of source signals from a given set

of combined signals [44]–[46]. The term 'blind' implies the absence of any prior knowledge regarding the source signals [45].

Among the prominent techniques for BSS, ICA stands out [44].

ICA is an algorithm for transforming a set of various signals into distinct and unrelated components. When ICA is applied to EEG data it is expected that certain components will closely resemble the original sources of signals, while others will likely represent undesired artifacts [44]. During the subsequent phase of feature selection, which is a critical step in signal processing before classification, the removal of features originating from "artifact components" becomes essential, while retaining those originating from components crucial for achieving accurate classification [44].

Therefore, the principles underlying the elimination of features associated with “artifact components” from the pool of features represents a critical issue. Artifacts can be broadly classified into two main types of activities. Some artifacts, such as those resulting from eye movements, display rhythmic patterns throughout each experimental trial. Conversely, certain artifacts, like unexpected body movements, appear at irregular intervals over the entire duration of the EEG recordings [44]. Given that both categories of artifacts are unrelated to the specific classes encoded within the recorded signals, they do not contribute to an increase in classification accuracy [44]. Therefore, in situations where precision in classification is a pivotal metric during the feature selection process, it is necessary to exclude features computed from components that mirror artifacts from the collection of features [44].

The problem tackled by ICA can be described as follows. Imagine a scenario where there are n linear combinations of n distinct components. The observed signals, represented by vector x , can be expressed as [44]:

$$x = As, \tag{1.1}$$

where A represents a mixing matrix with dimensions $n \times n$, and s is a vector containing independent components. The objective of ICA is to identify a matrix W , which essentially serves as the inverse of matrix A . This matrix W is used to undo or reverse the mixing effect. Once we have computed matrix W , we can then obtain the independent components through the following process [44]:

$$y = wX \cong s, \tag{1.2}$$

The majority of ICA algorithms impose certain conditions on the combined signals. The initial requirement pertains to the statistical separation of source signals s , the second involves a non-Gaussian distribution of these source signals, and the third condition is the equality between the number of source signals and mixture signals [44]. While the first two constraints serve as fundamental assumptions in numerous algorithms, the third condition is primarily introduced to simplify the algorithmic process [44].

Additionally, it is assumed that each source signal possesses unit variance, denoted as $E\{s_i^2\} = 1$. To maintain this assumption, the source signal matrix undergoes whitening before the ICA computation [44]. Another assumption, introduced solely for the purpose of simplifying the algorithm, is that all mixed signals are centered.

As previously mentioned, ICA functions without the necessity for prior knowledge of the source of signals. Instead, ICA algorithms rely on the concept of statistical independence among the mixed signals [44]. According to the formal definition, two variables, a and b , are considered independent if knowing the value of a imparts no information about the value of b , and vice versa [44] [46], [48]. Formally, independence can be defined in terms of the probability density function (pdf) [44] [47]:

$$f(x_1, x_2, \dots, x_m) = f_1(x_1)f_2(x_2) \dots f_m(x_m),$$

1.3

where x_1, x_2, \dots, x_m are random variables.

Two strategies exist for evaluating independence: maximizing non-Gaussianity and reducing mutual information. The majority of existing ICA algorithms adopt one of these approaches [44]. When employing the first strategy, the algorithm's objective is to transform the components in a manner that results in highly non-Gaussian distributed source signals (based on the assumption that stronger non-Gaussianity corresponds to stronger independence [44], [47]). In simpler terms, the distributions of the combined signals must exhibit greater Gaussian characteristics compared to the source signals. This approach involves the utilization of various metrics to quantify non-Gaussianity, such as kurtosis, negentropy, approximations of negentropy, and similar measures [44] [48].

In our study we used the FastICA, which is an ICA approach that utilize the non-Gaussianity maximization.

In the second strategy, mutual information is utilized. Mutual information measures the extent to which information about variable a can be inferred from information about variable b . As a smaller mutual information value implies that more information regarding a specific system is

contained within the variables [44], [47], ICA algorithms following this approach work toward minimizing the mutual information among the outputs of the system [44], [48].

1.6.2 SOUND

The SOUND algorithm is method that leverages the multi-dimensional characteristics of the data. It assess the dependability of each sensor by considering readings from all other sensors, and subsequently enhance the accuracy of the recorded data [17].

EEG and MEG record brain activity by assessing electromagnetic fields generated by post-synaptic currents, that represent the fundamental signal source currents. The signals collected from a set of s electrodes at different time points (T instances or samples) can be expressed as follows [17]:

$$Y = \bar{Y} + N = LJ + N, \tag{1.4}$$

where Y and \bar{Y} are $S \times T$ matrices holding the noisy and the noise-free data, respectively, while N is a $S \times T$ noise matrix. \bar{Y} can be written as a product of the $S \times J$ lead field matrix L and the $J \times T$ source-current matrix J , J is the number of all the sources [17]. The sensitivity of sensors s to source j is described by the element $l_{s,j}$ in L ; while j_j the j th row of J , covers the waveform of source j [17].

The aim is to estimate \bar{Y} from Y . To reach the goal, a minimally noisy source estimates, \hat{J} , is constructed and is then used to recreate the cleaned versions of the sensor signals, \hat{Y} . J could contain some uninteresting brain activity, that creates so-called neural-noise signals. Nevertheless, the aim here is not to separate the neural-noise component from the data, but rather to reduce as much as possible the amount of noise and artifacts (of extracranial origin), N , leaking into the source estimate \hat{J} [17].

If we possessed knowledge about how noise spreads across the sensor field, i.e., the noise covariance Σ , we should highlight the most reliable data directions in the estimation of source currents J . We accomplish this by multiplying the equation 1.4 from left with $\Sigma^{-1/2}$, which relate to whitening the data with respect to the noise [17].

$$(\Sigma^{-1/2})Y = (\Sigma^{-1/2})LY + (\Sigma^{-1/2})N = \tilde{Y} = \tilde{L}J + \tilde{N}, \tag{1.5}$$

where \tilde{Y} , \tilde{L} and \tilde{N} are the cleaned versions of the signal, lead-field, and noise matrix, respectively.

From the equation 1.5, J can be calculated as the Tikhonov-regularized minimum-norm estimate (MNE) [17]:

$$\hat{\mathbf{j}} = \tilde{\mathbf{L}}^T (\tilde{\mathbf{L}}\tilde{\mathbf{L}}^T + \lambda \mathbf{I})^{-1} \tilde{\mathbf{Y}}, \quad 1.6$$

where λ is regularization parameter.

To use the equation 1.6, we must know Σ . If we make the assumption that the noise is not correlated among the sensors, the noise covariance matrix transforms into a diagonal structure, $\Sigma = \text{diag}(\sigma_1^2 \dots, \sigma_s^2)$ and allows to estimate the noise level sigma, in each electrode s . The diagonality assumption simplifies the interpretation of the equations 1.4-1.6; when estimating \mathbf{J} , we give more importance to those channels that have better SNR.

If we knew $\bar{y}_{s,t}$, the noiseless dimension in electrode s at time t , then the noise level in s could be calculated easily as [17]:

$$\sigma_s = \sqrt{\frac{\sum_{t=1}^T (y_{s,t} - \bar{y}_{s,t})^2}{T}} \quad 1.7$$

If it can be demonstrated that we can accurately determine the source currents, we can then proceed to estimate the noise-free sensor signal $\bar{y}_{s,t}$ by [17]:

$$\hat{y}_{s,t} = l_s \hat{j}_{.,t} \quad 1.8$$

Replacing $\hat{y}_{s,t}$ results in the noise estimate $\hat{\sigma}_s$.

Equations 1.5-1.8 can serve to validate the signals obtained from various sensors through cross-validation. The noise level of sensor s' is evaluated using equation 1.8. We search for the most likely value for $\hat{y}_{s',t}$, given the measurements of all the other channels $y_{\neq s',t}$. We first find $\hat{j}_{.,t}$ by replacing $\tilde{\mathbf{Y}} = \tilde{\mathbf{Y}}_{\neq s'}$ and $\tilde{\mathbf{L}} = \tilde{\mathbf{L}}_{\neq s'}$ [17]. The noiseless signal in s' can be estimated by using equation 1.7 and then the noise level in the same electrode can be determined.

Then, we can continue assessing the noise level in any other channel s'' with the same approach. We now have enumerated the noise level in sensor s' , we can take this into account by updating $\hat{\Sigma}$ and cleaning the original data again to improve $\hat{j}_{.,t}$. From the improved version of $\hat{j}_{.,t}$, we now estimate the noise in sensor s'' [17].

However, if we want to estimate the noise in sensor s' , we must know the noise levels in all the other electrodes. The problem can be solved by evaluating each sensor many times in an iterative way, always updating $\hat{\Sigma}$ based on the new noise estimates.[17] After each step, the noise covariance and the channel-signal estimates become more precise.

To ensure an effective functioning of the proposed cross-validation approach the EEG data must be anchored to a high-quality channel reference before starting the iteration process. Failure to do so would result in the reference channel's noise contaminating all other channels, thereby contravening the assumption of uncorrelated noise. In the next section, we introduce an automated method for the selection of an appropriate reference channel [17].

In summary, the noise levels can be established by using this iterative procedure. Figure 7 provides a graphical representation of the iteration process [17]:

1. Change the reference of the data to a carefully chosen sensor with high quality recordings. Provide an initial estimation for $\hat{\Sigma}$ in the selected reference framework.
2. Continuously update the approximations for the values of $\hat{\sigma}_s$. In each iteration, compute a new $\hat{\sigma}_s$ value based on the following procedure:

$$\hat{\sigma}_s = \sqrt{\frac{\sum_{t=1}^T (y_{s,t} - l_s \hat{j}_{.,t})^2}{T}}, \text{ where}$$

$$\hat{j}_{.,t} = \tilde{L}^T_{\neq s} (\tilde{L}_{\neq s} \tilde{L}^T_{\neq s} + \lambda I)^{-1} \tilde{y}_{\neq s,t}$$

Update $\hat{\Sigma} = \text{diag}(\hat{\sigma}_1^2, \dots, \hat{\sigma}_s^2)$ after each iteration, and then reapply whitening to the original data

3. Reiterate step 2 until the sum has converged.
- 4.

To monitor the convergence of $\hat{\Sigma}$, we can calculate the relative variations in sensor-specific noise levels between consecutive full iteration rounds. Once the relative change in all channels falls below a predefined threshold, such as 1%, we can conclude the iteration process [17].

The last estimated noise covariance matrix can then be applied to whiten the original data. In the final step, we utilize the noise-reduced source estimates to create improved versions of the sensor-level signals. Consequently, the final refined dataset can be expressed as follows [17]:

$$\hat{Y} = L \left(\hat{\Sigma}^{-\frac{1}{2}} L \right)^T \left(\hat{\Sigma}^{-\frac{1}{2}} L L \hat{\Sigma}^{-\frac{1}{2}} + \lambda I \right)^{-1} \hat{\Sigma}^{-\frac{1}{2}} Y,$$

1.9

$$\lambda = \lambda_0 \text{trace}(\hat{\Sigma}^{-\frac{1}{2}} L L \hat{\Sigma}^{-\frac{1}{2}}) / S.$$

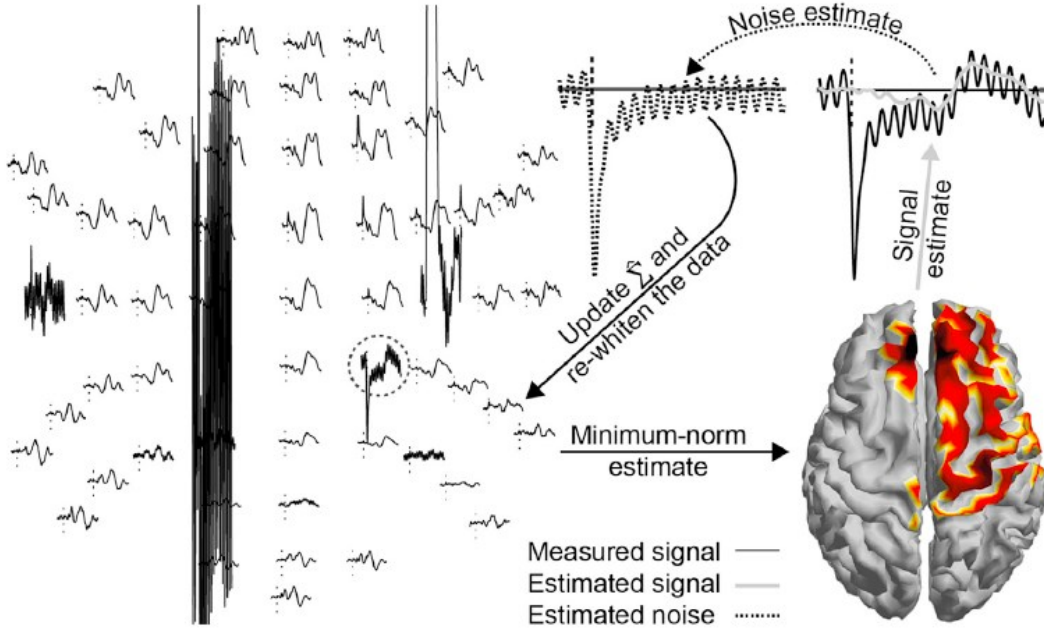


Figure 7: Representation of one iteration step in SOUND [17].

1.6.3 SSP-SIR

One way to effectively remove artifacts and noise from neurophysiological data is by excluding the signals recorded from corrupted channels from further analysis. This represents a robust and intuitive approach, especially when these disruptions are limited to a small number of problematic channels. However, eliminating a channel reduces data dimensionality by one. For instance, if we reject two channels from a 60-channel EEG dataset, we can hypothetically estimate a maximum of 58 degrees of freedom for cortical activity (or 57 when using average reference) [49]. However, this strategy becomes impractical when artifacts are simultaneously present in multiple channels. Nevertheless, even when artifactual activity is distributed across several channels, it can often be characterized by a few spatial patterns that fluctuate in amplitude over time but maintain their spatial configuration. In such cases, it is still possible to moderately reduce the data's dimensionality to eliminate undesired signals [49].

Assuming that the whole EEG recordings are described by a linear model with matrix notation as [49]:

$$Y(t) = LJ(t) + M_A S_A(t) + M_N S_N(t),$$

1.10

where the element L_{ij} defines the sensitivity of sensor i to the cortical equivalent source j . L is the neuronal lead-field matrix: the rows describe the sensitivity profiles of different EEG

sensors to all the possible cortical sources while the columns of L delineate the scalp voltage patterns or spatial distributions created by distinct localized cortical current sources [49].

M_A and M_N are the artifact- and noise-mixing matrices, and S_A and S_N are the artifact- and noise-signal matrices. The columns of mixing matrices represent the spatial patterns of various interfering signal components, while the rows of signal matrices contain the temporal profiles or time courses of these corresponding components. When examining the linear model for our recordings, it becomes evident that the spatial patterns of various signal components, such as the columns of the lead-field and mixing matrices, remain constant over time [49].

Nonetheless, some signal elements could exhibit greater prominence during specific moments or at particular frequencies, as evidenced by the temporal profiles $J(\mathbf{t})$, $S_A(\mathbf{t})$, and $S_N(\mathbf{t})$. The concept behind signal-space projection (SSP) is to leverage these temporal fluctuations to recognize the artifact patterns that can subsequently be removed [49].

For instance, if we observe that a specific time segment or frequency band predominantly is contaminated by artifacts, we can utilize this specific dataset portion to estimate the artifact patterns that should be eliminated [49].

When considering TEPs, our focus lies on eliminating muscle artifacts induced by the magnetic stimulation, which occur concurrently with the initial cortical responses to TMS. Nonetheless, brain-related activity typically presents itself in EEG data at frequencies below 100 Hz, whereas muscle activity exhibits a broader frequency range. Therefore, by applying a high-pass filter to the TMS-EEG data, we can emphasize the presence of muscle activity [49].

$$H(Y(t)) = LH(J(t)) + M_A H(S_A(t)) + M_N H(S_N(t))$$

$$H(Y(t)) \approx M_A H(S_A(t)) + M_N H(S_N(t))$$

$$H(Y(t)) = USV^T$$

1. 11

where $H(\cdot)$ represents a high-pass filter while USV^T is the singular value decomposition of the high-pass filtered data. If we can make the assumption that the noise is largely uncorrelated, the topographies (represented by column vectors of \mathbf{U}) associated with the k most prominent singular values should account for the majority of the muscle artifacts. [49]

Note that none of the individual vectors U_k , where $k = 1, 2, \dots, n$, needs to precisely match an underlying muscle artifact component. It is sufficient that a linear combination of these

singular vectors can account for the actual artifact patterns. In other words, we can say that these singular vectors collectively define the muscle artifact subspace. [49] If the k most significant singular vectors U_k encompass the artifact-related signal space, we can express the spatial filter W_{SSP} for muscle artifact removal as [49]:

$$\begin{aligned} U_k S_k V_k^T &\approx M_A H(S_A(t)) \\ W_{SSP} &= I - U_k U_k^T, \end{aligned}$$

1. 12

resulting in $W_{SSP} M_A \approx 0$. Therefore, we can express the EEG signal after muscle artifact reduction as [49]:

$$W_{SSP} Y(t) \approx W_{SSP} L J(t) + W_{SSP} M_N S_N(t)$$

1. 13

The drawback of SSP lies in its potential to alter neuronal patterns [50]. Similarly, to the process of rejecting problematic channels, when we eliminate specific signal directions to mitigate artifact signals, the data representation undergoes a transformation. However, this transformation is relatively straightforward to grasp in the case of channel removal, and we can easily fill in the gaps for data visualization. Conversely, when we exclude muscle artifact patterns from EEG data, the alterations in the EEG representation of brain activity become more abstract [49]. Moreover, EEG is often visualized using topographical plots, which have a direct connection to the physical world; the colours at electrode locations correspond to measured voltages. After applying SSP, this intuitive connection is lost because the rows of EEG data no longer represent distinct EEG channels. Instead, each row in the data matrix represents a linear combination of the original channel signals. Therefore, to regain a physical understanding of EEG after SSP, we must interpolate the abstract signal directions that were removed [49].

Source-informed reconstruction (SIR) is a method that leverages the head's forward model to interpolate the signal directions removed by SSP [49] [18]. While the dimensions of the projected signals may appear abstract, they are precisely defined within the W_{SSP} operator. This information can be considered when estimating the cortical brain activity $\hat{J}(t)$ that generated the artifact-suppressed versions of EEG [49]:

$$\hat{J}(t) = (W_{SSP} L)^+ W_{SSP} Y(t),$$

1. 14

In the equation provided, where $(\cdot)^+$ represents the pseudoinverse operation, a widely employed technique in EEG analysis for constructing the pseudoinverse involves using minimum-norm estimation [49] [51]. Using the forward model, we can recreate the sensor signals within the original EEG channels using the current estimates that have been freed from artifacts. This can be accomplished by multiplying the cortical current with the lead-field matrix, resulting in [49]:

$$\hat{Y}(t) = L\hat{J}(t).$$

1. 15

Consequently, we can encapsulate the SSP-SIR procedure in a single equation [49]:

$$\hat{Y}(t) = L(W_{SSP}L)^+W_{SSP}Y(t) = W_{SSP-SIR}Y(t).$$

1. 16

The concept behind the integrated SSP-SIR approach is showed in Figure 8. Since its introduction, SSP-SIR has been widely employed in various TMS-EEG investigations to effectively reduce muscle artifacts induced by TMS [49] [7], [52]–[54].

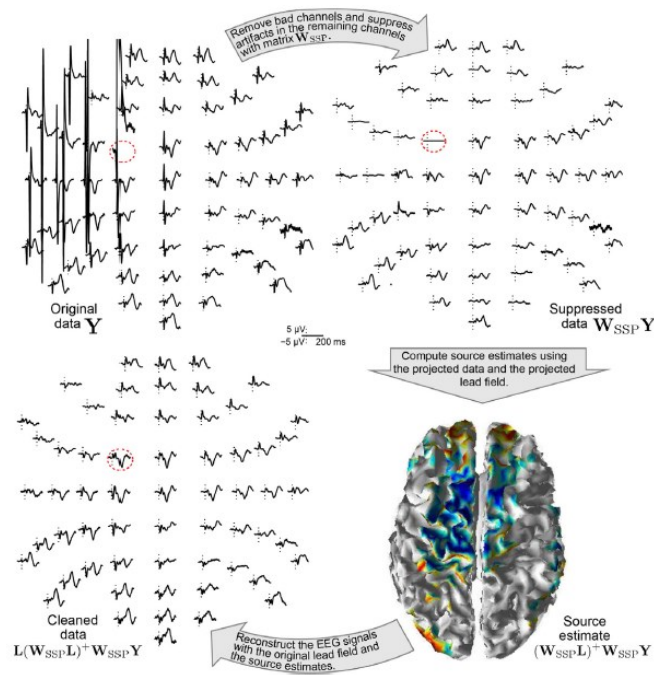


Figure 8: The principle of SSP-SIR [18].

The application of SSP-SIR extends beyond addressing TMS-induced muscle artifacts, and it has been used to tackle various other issues [49]. As an example, Biabani et al. [55] and Fernandez et al. [56] employed the SSP-SIR method to reduce sensory artifacts associated with TMS. Additionally, the SIR method has been also used to interpolate the excluded noisy

channels, as demonstrated by Nieminen et al. [57]. This SIR-based channel interpolation is an integral component of the SOUND algorithm [49].

1.7 Source Localization

The primary objective of functional neuroimaging techniques is to localise specific brain regions involved in particular activities. Functional magnetic resonance imaging (fMRI) is proficient in this task but has several limitations. Its temporal resolution is relatively low, and brain activity is assessed indirectly, hindering precise evaluation when brain regions activate in response to a given stimulus [58].

On the other hand, both the EEG and MEG signals directly capture brain activity with remarkable temporal precision. However, the use of EEG as a neuroimaging tool is complex because neural signals are recorded from the scalp's surface, and it is challenging to localize the source of the electrical signal, i.e., to precisely determine the population of cortical neurons generating the signals recorded by the electrodes [58]. This complexity arises from the fact that various configurations of neural circuits could potentially generate the electrical potentials recorded at the scalp.

Therefore, to employ EEG for source localisation and visualisation a necessary step is to reconstruct the sources of the signals detected by the scalp electrodes. Achieving this requires addressing two key challenges: the forward problem and the inverse problem [44] [61].

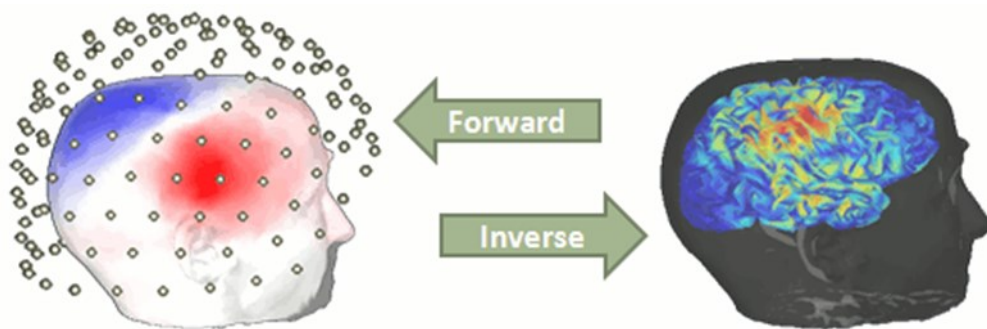


Figure 9: Graphical representation of the two processes involved in current localisation: the forward and inverse problems[59].

The two problems are intrinsically connected, but the forward problem must be solved before the inverse problem. Finding the electric potentials at the scalp electrode given a configuration of dipole sources in the brain means solving the forward problem[58].

On the other hand, finding the source that generated the electric potential recorded by the electrode means solving the inverse problem [58].

In the following sections we provide the mathematical solution of both problems.

1.7.1 The forward problem

As previously mentioned, the primary source of EEG signals recorded by the electrodes placed on the surface of the scalp is represented by the pyramidal neurons within the cerebral cortex. These neurons generate the EEG signal through post-synaptic currents flowing across their apical dendrites, which are mainly oriented perpendicular to the brain surface [58], [60].

During an excitatory impulse, neurotransmitters initiate a flow of positive ions into the post-synaptic membrane. This, in turn, leads to changes in electrical charges within and around the neuron, encompassing the cell body, apical dendrite, and the surrounding extracellular space. The currents and fields in this system behave as if they were stationary at every instant, i.e., they display a quasi-stationary behaviour [61]. Furthermore, a group of neurons operating in synchronization can be represented as an electrical dipole.

The aim is to find the electric potential V measured by an electrode with position on the scalp r generated by an electric dipole d at position r_{dip} in a reasonable time.

This implies finding N potentials $V(r)$, corresponding to the number of electrodes on the scalp, generated by different configurations of p dipoles d and position r_{dip} .

We must then find the solution to the system of equations given by:

$$V = \begin{bmatrix} V(r_1) \\ \vdots \\ V(r_N) \end{bmatrix} = \begin{bmatrix} g(r_1, r_{dip_1}, e_{d_1}) & \cdots & g(r_1, r_{dip_p}, e_{d_p}) \\ \vdots & \ddots & \vdots \\ g(r_N, r_{dip_1}, e_{d_1}) & \cdots & g(r_N, r_{dip_p}, e_{d_p}) \end{bmatrix} = G \left((r_j, r_{dip_1}, e_{d_i}) \right) \begin{bmatrix} d_1 \\ \vdots \\ d_p \end{bmatrix} \quad 1.17$$

Rewritten in matrix form and adding a noise matrix n , the forward problem can be summarised as:

$$V = GD + n \quad 1.18$$

where G is the gain matrix and D the electric dipole matrix.

For a more detailed discussion please refer to the article by Hallez et al. [62].

Several analytical methods have been applied to solve the forward problem.

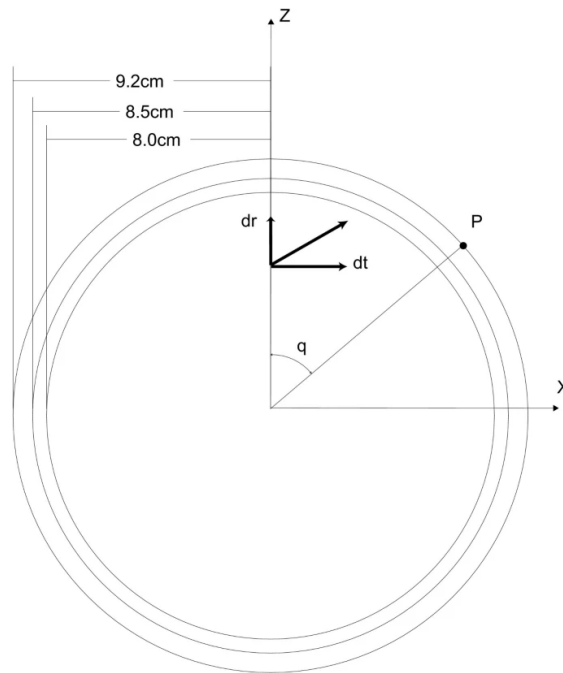


Figure 10: Spherical head model with three concentric circles [62].

A first analytical model to the solution of 2.35 used a spherical head model, divided into three concentric circles (Figure 10). The innermost circle represents the brain, the middle the skull and the outermost represents the scalp. Each circle has a different radius and conductivity. Given a dipole on the z axis and a point P on the scalp in the xz plane, it is possible to derive the electrical potential V at point P [58].

Starting from this simplistic model, increasingly realistic head models were introduced and provided a more accurate description of the conductive properties of the head, thereby increasing the accuracy of the estimation.

The Boundary Element Method (BEM) consists of calculating the electrical potential V at the interface between different compartments with different conductivities, where the final interface lying between a conducting and a non-conducting volume, i.e., air. Therefore, this technique consists in dividing the brain into finite elements with different conductive properties, where the electrical potential at the electrode V can be derived. Figure 11 shows the division of different head regions into finite elements, each describing the conductive properties of a tissue, and the head model used. In this model, three types of interfaces can be distinguished: brain-skull, skull-scalp and scalp-air [62].

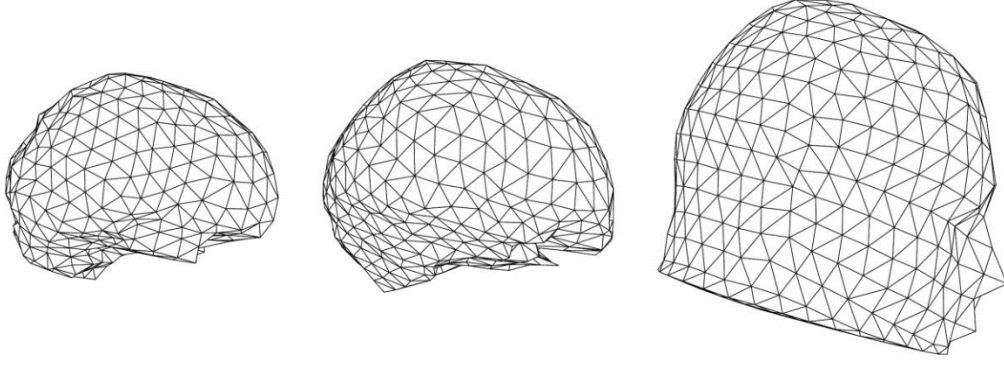


Figure 11: Mesh of a human head used in BEM. The surfaces indicate a brain-skull, skull-scalp, scalp-air interface [62].

The limitation of this resolution method stems from the assumption that the regions used to represent different types of tissue are homogeneous and isotropic. This simplification does not accurately represent the complexity of the human head, where various tissues and regions exhibit anisotropic conductivity characteristics. However, it offers a computational advantage compared to other approaches [58], [62].

Conversely, the Finite Element method (FEM) aims to address the forward problem by applying boundary conditions and dividing the head model into small volumetric elements.

Once the forward problem is solved, the subsequent step involves tackling the inverse problem [58].

1.7.2 The inverse problem

While the forward problem involves the measurement of electrical potential V generated by multiple dipoles, the inverse problem is focused on identifying the sources responsible for the potentials recorded by the electrodes [63].

Given a discrete time series T , N electrodes and M electrical potential measurements at the electrodes, one must find the p dipoles that satisfy the equation derived from the forward problem [58], [63]:

$$M = \begin{bmatrix} m(r_1, 1) & \cdots & m(r_1, T) \\ \vdots & \ddots & \vdots \\ m(r_N, 1) & \cdots & m(r_N, T) \end{bmatrix} = \begin{bmatrix} g(r_1, r_{dip_1}) & \cdots & g(r_1, r_{dip_p}) \\ \vdots & \ddots & \vdots \\ g(r_N, r_{dip_1}) & \cdots & g(r_N, r_{dip_p}) \end{bmatrix} \begin{bmatrix} d_{1,1}e_1 & \cdots & d_{1,T}e_1 \\ \vdots & \ddots & \vdots \\ d_{p,1}e_p & \cdots & d_{p,T}e_p \end{bmatrix}$$

1. 19

is summarised in its matrix form:

$$M = GD + n,$$

1. 20

where M is the matrix of measured data at T instants, G is the gain matrix, n is the noise matrix and D is the matrix of electric dipoles at T instants.

Therefore, the solution of the inverse problem consists in finding the estimate of the dipole matrix, knowing the matrix M from the measurements, and G , from solving the forward problem [63].

However, the inverse problem has intrinsic limitations, since the number of dipoles within the human brain is much greater than the number of electrodes applicable on the scalp, i.e., $p \gg N$. Therefore, no single solution can be achieved, meaning that a different combination of active sources can reproduce the same signal measured by the EEG system [63].

1.7.2.1 Parametric and non-parametric approach for the inverse problem resolution

Inverse problem-solving methods can be divided into two categories: parametric and non-parametric. The former estimates the position of electric dipoles from a defined number of dipoles assumed *a priori*. The latter estimate the orientation and magnitude of electric dipoles distributed at fixed points in the brain. Therefore, the first distinction between the two approaches turns out to be what is estimated: in the former the position, the force and direction, in the latter only the force and direction [58].

In non-parametric methods, the values to be estimated are the force and direction of the electric dipole. Therefore, solving the inverse problem reduces to a linear problem and in equation 1.19 the parameters r_{dip_i} and e_i are known *a priori*.

On the other hand, parametric methods propose to estimate the position of the dipoles directly. This leads to having to solve a non-linear equation system, since the parameters r_{dip_i} and e_i appear in the equation non-linearly. To make it possible to solve by this method, it is necessary to make an *a priori* assumption about the number of dipoles present, the larger this number the greater the computational cost of these techniques [58].

Different methods have been used in the literature to solve the inverse problem. The most frequently used are: Minimum Norm Estimation (MNE), Low Resolution Brain Electromagnetic Tomography (LORETA) and dynamic Statistical Parametric Mapping (dSPM) [64].

In particular, by choosing $Var[D]$ proportional to $(W.W^T)^{-1}$ where W is a covariance matrix $p \times p$, we obtain a family of smooth estimators which contain LORETA and MNE methods as particular cases. For this case the minimization problem of Eq. 1.19 becomes [64]:

$$\hat{D} = \underset{D}{\operatorname{argmin}} [\|M - G.D\|^2 + \alpha \|W.D\|^2]$$

1. 21

Where \hat{D} is the estimation of D . For this problem, the solution is known to have the closed form:

$$\hat{D} = (G^T.G + \alpha W^T.W)^{-1}.G^T.M$$

1. 22

Minimum Norm Estimate

The MNE (Minimum Norm Estimate) solution is achieved when W is configured as the identity matrix I_p in equation 1.21. This approach assumes that the solution to the inverse problem should aim to minimize energy [64].

LORETA

By modifying the covariance matrix W in the closed solution 1.21 to incorporate the Laplacian operator, we can derive LORETA. This adjustment effectively links adjacent vertices in the brain mesh, leading to a reduction in discrepancies between coefficients associated with neighbouring sources. As a result, it generates more uniform current-source estimates, promoting smoothness in the estimations [64].

Materials and Methods

2.1 Subjects

The dataset used in this study was acquired as a part of a larger TMS–EEG study to investigate differences in cortical excitability and connectivity in a group of patients diagnosed with mild cognitive impairment (MCI) with respect to a control group of age- and gender-matched healthy subjects.

A total of five healthy subjects were recruited. All the participants were right-handed and did not have major neurological or psychiatric disorders and underwent neuropsychological testing to exclude cognitive impairment. No participant was taking drugs known to influence M1 excitability or had contraindications to the use of TMS according to the latest international guidelines on the safety of the technique [20]. All subjects underwent a brain MRI for 3D brain reconstruction and neuro-navigation required for the TMS-EEG application.

The study protocol was approved by the local Research Ethical Committee, and it was carried out in accordance with the latest version of the Helsinki Declaration.

Demographic, clinical, and neurophysiological characteristics of the included participants are shown in Table 2.

Table 2: Demographic, clinical, and neurophysiological characteristics of participants. MMSE: Mini Mental State Examination (score corrected for age and education), RMT: resting motor threshold, MSO: maximum stimulator output.

	<i>Subject 01</i>	<i>Subject 02</i>	<i>Subject 03</i>	<i>Subject 04</i>	<i>Subject 05</i>
Age (years)	80	79	70	72	67
Gender	M	M	M	M	M
MMSE score	27	26	30	26	26
Education (years)	10	13	20	18	8
RMT (%MSO)	50	40	43	38	56

2.2 Instrumentation

2.2.1 Transcranial magnetic stimulation

Single-pulse TMS was delivered using a Nexstim system (Nexstim, Helsinki, Finland) connected to a figure-of-eight coil, provided with reflective markers for neuro-navigation.

The coil was placed tangentially to the scalp and turned backwards at 45° to the midline, in order to induce currents in the posterior-anterior direction.

TMS was delivered over the M1 “hotspot”, defined as the scalp position where TMS elicited the largest MEPs in the contralateral first dorsal interosseous (FDI) muscle. This location was sampled in the space separately for each hemisphere by mapping the M1. During the stimulation the coil was maintained in the correct position throughout the stimulation by using a 3D infrared tracking position sensor unit (Polaris, Northern Digital Inc., Waterloo, Canada) integrating a T1-weighted MRIs recorded from all patients [65].

Resting motor threshold (RMT) was defined as the lowest stimulation intensity required to elicit MEPs of ≥ 50 μ V peak-to-peak amplitude in at least 5 out of 10 consecutive trials, in the relaxed FDI muscle. RMT was measured separately for each M1. The stimulation intensity was set at 120% RMT. The EMG activity of the FDI was recorded through a pair of Ag/AgCl 10 mm cup electrodes placed over the muscle contralateral to the stimulated M1, arranged in a belly-tendon montage. Raw EMG signal was sampled at 3kHz, amplified, and bandpass filtered between 10 and 500 Hz and then digitized at 5kHz.

2.2.2 Electroencephalographic recording

EEG was recorded using a TMS-compatible amplifier NeurOne Tesla (Bittium Biosignals Ltd., Kuopio, Finland) from 62 passive electrodes mounted on an elastic cap (EASYCAP, Easycap GmbH, Am Anger 5, DE-82237 Woerthsee, Germany), according to the international 10-10 system, including: Fp1 Fp2 F3 F4 C3 C4 P3 P4 O1 O2 F7 F8 T7 T8 P7 P8 Fz Cz Pz Iz FC1 FC2 CP1 CP2 FC5 FC6 CP5 CP6 TP9 TP10 F1 F2 C1 C2 P1 P2 AF3 AF4 FC3 FC4 CP3 CP4 PO3 PO4 F5 F6 C5 C6 P5 P6 AFz FCz FT7 FT8 TP7 TP8 PO7 PO8 Fpz Cpz POz Oz. The reference electrode was placed outside the EEG cap, on the forehead, 2 cm above the nasion. In the offline analysis, an average reference was used. All electrodes were grounded at AF7. Impedances for each channel was kept below 5 k Ω . EEG signal was bandpass filtered (DC-2.5 kHz) and sampled at 5kHz. An anti-aliasing hardware filter was also applied, with a cut-off frequency of 1250Hz. In order to mask TMS clicks and avoid possible AEPs (Auditory Evoked Potentials), participants wore earphones continuously playing a customized masking noise. Additionally, a pair of electrodes were placed close to the left eye (EOG) to monitor ocular artifacts (blinks and eye movements).

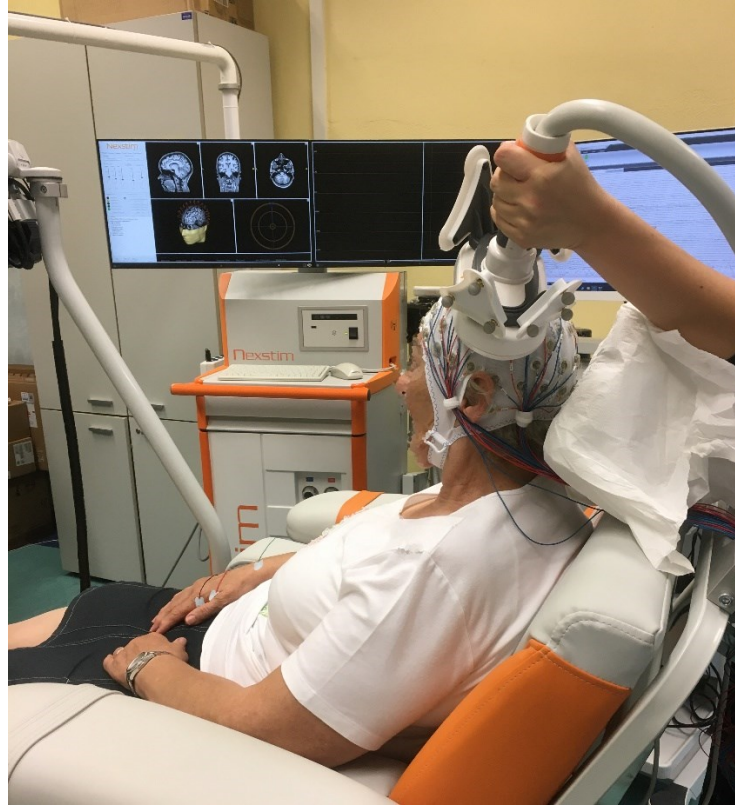


Figure 12: TMS-EEG experimental setting.

2.3 Experimental Protocol

All the experimental sessions were carried out at the Neurology Clinic of the University Hospital in Padua.

The individual MRIs required for the 3D reconstruction and navigation were scanned with 1.5 T (T1-weighted; 1 mm thickness; sagittal orientation) for each subject were obtained prior to the TMS-EEG assessment.

At the beginning of each session, after the EEG montage and impedance check, a resting EEG was recorded for five minutes, asking the subjects to relax and to keep their eyes closed. The EEG signal was continuously monitored during the recordings to minimize motion artifacts and check for electrode integrity.

During the TMS stimulation, subjects were comfortably sitting on an electronically adjustable chair designed for TMS (Nextstim, Helsinki, Finland) with their forearms resting on armrests. Participants were asked to keep their eyes open and to fixate a specific marker placed at a distance of about 70 cm. All subjects underwent TMS stimulation of the M1 of both hemispheres. After the identification of the hotspot and the definition of the RMT, 120 TMS

stimuli at an intensity of 120%RMT were delivered separately for each hemisphere in a randomized order. Single TMS pulses were applied with an inter-pulse interval randomly jittering between 1,5 and 1,8 s, which does not affect longitudinally recorded TEPs [10].

2.4 Data processing

Offline EEG pre-processing was performed with EEGLAB v2023.0 with the addition of some functions included in the TMS-EEG signal analyser (TESA) toolbox [16] and in Brainstorm, an open-source MATLAB toolbox [59]; all running in MATLAB environment (MathWorks Inc., Natick, USA).

2.4.1 Pipelines

In the present work, TEPs were analysed using three different pre-processing pipelines applied using the TESA toolbox: Leodori et.al, Rogasch et.al and Mutanen et. al. The first two use the FastICA as a core function, while the third uses SOUND algorithm combined with the SSP-SIR method.

The pipelines are outlined in Table 3. Of note, the first three steps are shared among all the pipelines: after having loaded the datasets, we set the channels location using a MNI coordinate file for BEM model.

We then remove unused electrodes that in our case are EOG and EMG. In the following sections we will provide a detailed description of the applied pipelines.

Table 3: The three pipelines involved in the study.

<i>Leodori et. al</i>	<i>Rogasch et. al</i>	<i>Mutanen et. al</i>
Load dataset	Load dataset	Load dataset
Look-up channels location	Look-up channels location	Look-up channels location
Remove unused electrodes	Remove unused electrodes	Remove unused electrodes
Extract epochs [-1.3 1.3] s and demean [-100 -10] ms	Channels rejection	High pass filter 1-500 Hz
Remove stimulation artefact [-5 13] ms	Extract epochs [-1 1] s and demean [-100 -10] ms	Extract epochs [-1 1] s
Interpolate removed data	Remove stimulation artefact [-5 13] ms	Remove stimulation artefact [-5 13] ms
Band-pass filtering 1-500 Hz	Interpolate removed data	Interpolate removed data
Downsampling 1000 Hz	Downsampling 1000 Hz	Baseline correction [-100 -10] ms
Stimulation artifact [-5 13] ms removal	Bad trials rejection	SOUND algorithm
Bad trials rejection	Stimulation artifact [-5 13] ms removal	Bad trials rejection
FastICA 1 st round (large artifacts removal)	FastICA 1 st round (large artifacts removal)	ICA (removal of ocular artifacts)
Interpolate removed data	Interpolate removed data	Stimulation artefact [-5 13] ms removal
Band-pass 1-100 Hz and band-stop 48-52 Hz filtering	Band-pass 1-100 Hz and band-stop 48-52 Hz filtering	SSP-SIR
Epochs extraction [-1 1] s and demeaning [-100 -10] ms	Stimulation artifact [-5 13]ms removal	Interpolate removed data
Stimulation artifact [-5 13] ms removal	FastICA 2 nd round (all artifacts)	Band-pass 1-100 Hz and band-stop 48-52 Hz filtering
FastICA 2 nd round (all artifacts)	Interpolate removed data	Re-referencing to the average
Interpolate removed data	Bad channel interpolation	Downsampling 1000 Hz
Re-referencing to the average	Re-referencing to the average	Baseline correction [-100 -10] ms
Plot for quality check	Baseline correction [-100 -10] ms	Plot for quality check
	Plot for quality check	

2.4.1.1 *Leodori et. al*

This pipeline is inspired by the Rogasch et. al pipeline [16], explained in the next section. This pipeline it's one of the most validated in the literature, in particular it's been used by Leodori's research group[15].

We firstly extracted epochs extending from -1.3 to 1.3 milliseconds, slightly longer than the epochs that will be extracted later, preventing potential edge artifacts. Simultaneously, we applied data demeaning by subtracting the average of the entire epoch. This helps eliminate DC offsets.

Then, we removed data around the TMS pulse within the time range of -5 to 13 milliseconds. To ensure smooth data transitions, we employed cubic interpolation within this interval, reducing the risk of creating disruptive ringing artifacts during subsequent filtering. We implemented a primary frequency filter from 1 to 500 Hz, with the aim of eliminating low frequencies below 1 Hz. Of note, it is a fourth-order Butterworth filter, like all the others frequency filters used in the three pipelines.

To streamline computational demands, we downsampled the data to 1000 Hz. This step proves particularly advantageous when dealing with high-rate data, such as our case with a 5 kHz sampling rate.

Before applying the FastICA, we temporarily replaced the interpolated TMS-pulse data with zero values. In fact, replacing interpolated data around TMS pulse with constant amplitude data is necessary prior to ICA to improve performance [16]. We reinstated the interpolation right after ICA to ensure that this redundant information doesn't interfere with the algorithm.

We manually scrutinize EEG recordings to identify and remove problematic trials, a crucial step that significantly enhances the quality of ICA decomposition, especially when dealing with substantial, non-recurring artifacts like intense jaw clenching or head scratching.

We finally run FastICA, this function ranks and sorts the components by percentage variance explained by each time course. We then manually classified the components as artifacts or not obtaining a new dataset.

The first ICA stage, dedicated to the removal of large amplitude artifacts (such as TMS-related muscle, decay and movement) sets the stage for subsequent band-pass and band-stop filtering, further enhancing the second ICA decomposition process [66]that aims to eliminate the remaining artifacts.

Between the two ICA runs, we also extracted shorter epochs within the time frame of -1 to 1 millisecond to avoid cutting-edge artifacts.

Finally, we applied an average reference to complete the process.

2.4.1.2 Rogasch et. al

This pipeline, first developed by Rogasch [16] shares several similarities with the previous pipeline but also displays some differences. The primary distinction lies in our implementation of an automatic channel rejection early in the process, followed by interpolation after the completion of the two rounds of ICA. Consequently, all the preprocessing steps analyse fewer electrodes than the actual total count.

Epoch extraction occurs just once, within a time interval spanning from 1 to -1 s. Unlike the previous pipeline, we skip the application of a band-pass filter in the range of 1 to 500 Hz, leaving the slow decay artifacts removal to the ICA.

Additionally, a baseline correction is applied in the end, spanning from -100 to -10 ms.

2.4.1.3 Mutanen et. al

Like Leodori et. al, the Mutanen et. al pipeline initiates with a 1 Hz high-pass filter to avoid slow decay artifacts. Then, epochs from -1 to 1 second are extracted. However, the baseline correction is performed as a later step, before the SOUND algorithm application. The removal of TMS-induced artifacts is performed between -5 and 13 ms around the TMS stimulus artifact, and involves cubic interpolation. This step is essential to prevent a significant influence of the TMS-pulse artifacts on SOUND's noise estimation process, possibly compromising the efficacy in signal cleaning [1], [17].

After baseline correction, the SOUND algorithm was applied. To facilitate MNE integration in the cleaning process, SOUND necessitates a forward head model [67]. Importantly, two input parameters have a significant impact on cleaning outcomes of the SOUND algorithm. Firstly, the number of iterations, determining noise evaluation in each channel, which was set at 5 iterations to ensure convergence in the 62-channel EEG system [67]. Secondly, the lambda (λ) value was set at 0.1. This parameter regulates the extent of the cleaning process: a higher λ value results in greater noise removal but also raises the potential for excessive correction (over-cleaning) [67].

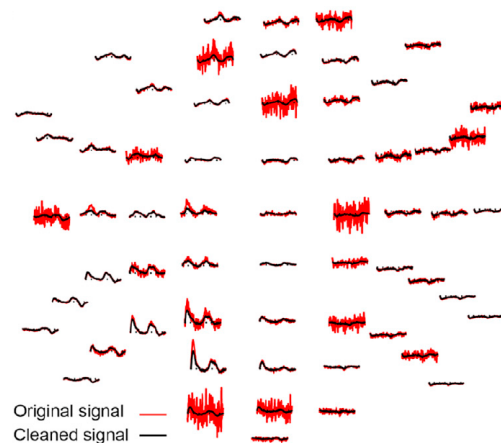


Figure 13: An illustration of TMS-EEG data, both before and after applying the SOUND correction, is depicted here. The underlying red curves represent the initial data, while the black curves represent the data post-SOUND correction [67].

Then we rejected bad trials via visual inspection. Subsequently, we apply the only ICA step, aiming to remove ocular artifacts considering their relative independence from TMS-evoked brain signals [1]. TMS pulse interpolation, is replaced with zero values, and later re-interpolated after the SSP-SIR procedure.

The SSP-SIR algorithm is then applied, with the aim to suppress TMS-induced muscle artifacts. The artefact dimensions were chosen manually from the `tesa_sspsir` function visualisation (see Figure 15). It corresponds to the number of Principal Components with greater high-frequency activity in the data that we want to delete. This process hinges on estimating the muscle artifact subspace from high-frequency components (>100 Hz) in the data. Accordingly, it is crucial not to impose aggressive low-pass filtering before SSP-SIR. [67] Furthermore, it is advisable to maintain a higher cutoff frequency, higher than 200 Hz, before applying SSP-SIR [67]. Hence, a band-pass filter from 1 to 100 Hz and a band-stop

filter from 48 to 52 Hz are applied at this stage after the execution of the SSP-SIR algorithm [1].

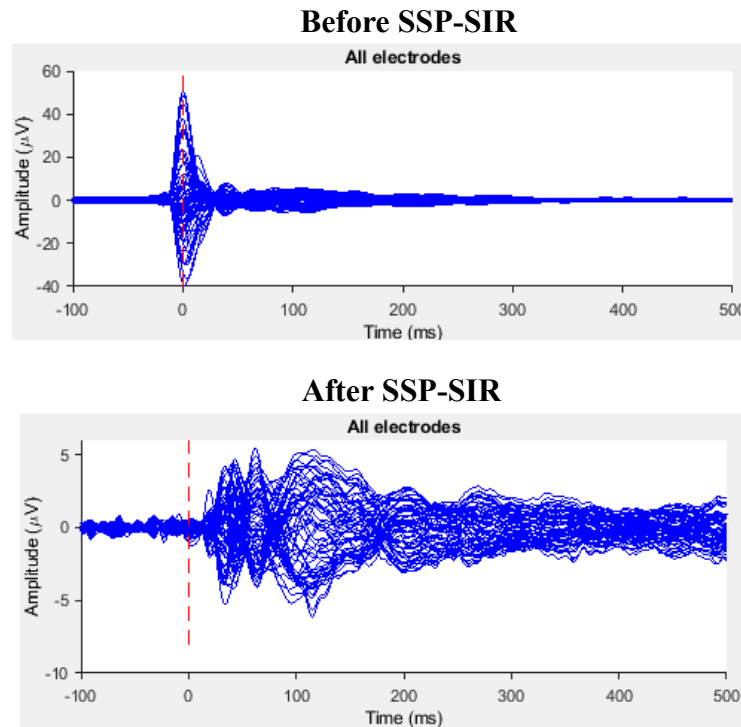


Figure 14: Illustration of TMS-EEG data both prior to and following the application of SSP-SIR to reduce muscle artifacts[67]. Note the different amplitude scale.

Then, data were re-referenced to the average, down-sampled to 1000 Hz, and baseline correction within the time interval of -100 to -10 ms was performed [1].

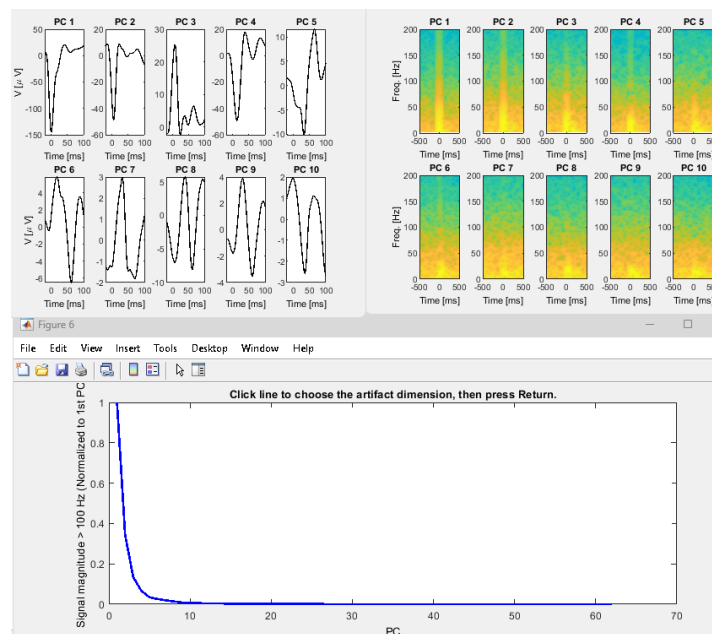


Figure 15: Selecting the artifact measurements manually from the tesa_spsir visualization [67].

Figure 15 displays the Principal Components (PCs) identified by the SSP-SIR algorithm. In the upper left panel the average time courses of various PCs are shown, while the upper right

panel displays the time-frequency representations of these PCs. The bottom panel illustrates the magnitude of high-frequency activity accounted for by different PCs.

In this specific instance, these three visualizations indicate the necessity to eliminate four PCs, which correspond to artifact-related dimensions. The first four PCs show pronounced and sharp responses immediately following the TMS pulse, which is characteristic of muscle artifacts. Furthermore, these components present broad frequency responses, encompassing frequencies that exceed the typical range for physiological brain-related EEG activity.

The last figure highlights that these two components predominantly account for the high-frequency signal, implying that by removing them we could effectively eliminate a significant portion of the artifactual muscular activity from the data [67].

2.6 Toolboxes

2.6.1 TESA

To address the challenges of reproducibility in offline TMS-EEG analysis, various open-source TMS-EEG analysis toolboxes have been developed, including TESA (TMS-EEG Signal Analyzer)[14], which was utilized in this study. TESA offers a standardized library of offline analysis methods commonly used in TMS-EEG research and was created as a plugin (extension) to EEGLAB, A widely used EEG analysis toolkit that operates on the MATLAB platform and is freely available for public use [14]. Integrating TESA within EEGLAB provides several advantages [14]. Firstly, EEGLAB already contains a wide range of functions for EEG analysis that can be utilized in conjunction with TESA functions. Secondly, EEGLAB's modular framework allows for flexible design and implementation of analysis pipelines [14].

2.6.2 Brainstorm

Brainstorm is an open-source MATLAB tool designed for collaborative use, specifically tailored for the examination of brain recordings encompass various neuroimaging methods such as MEG, EEG, fNIRS, ECoG, and multiunit electrophysiology [59]. For the purpose of this study, Brainstorm was used for the source localization, since it offers many options and intuitive visualizations.

Brainstorm offers three extensively documented categories of approaches for source localization: minimum-norm imaging, beamforming, and dipole modelling [59].

One notable common advantage shared among these methods is their computational efficiency, even when dealing with large datasets. These techniques derive estimates of brain source activity by applying a linear combination of sensor recordings. Brainstorm accomplishes this by calculating a kernel, essentially a large matrix, which can be stored in the database. This matrix can then be multiplied with sensor data arrays to generate source time series, either at specific brain locations or across the entire brain [59].

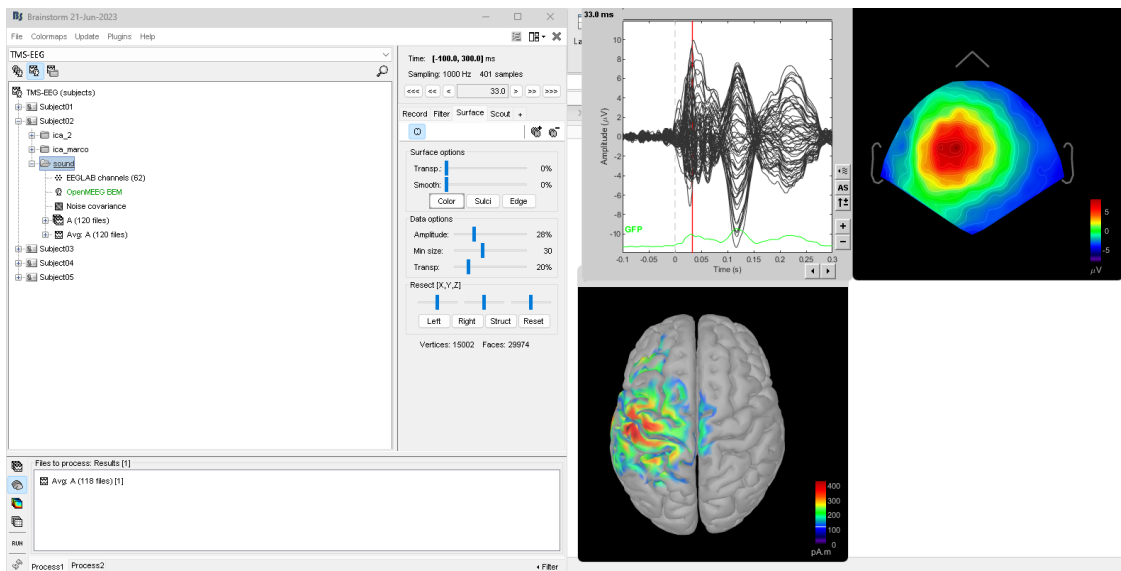


Figure 16: Brainstorm interface; with an example of TEPs, topography and source visualizations at latency 33 ms of one of our datasets.

For this thesis a default BEM model was used. The anatomical representation provided by the Brainstorm interface is shown in figure 17.

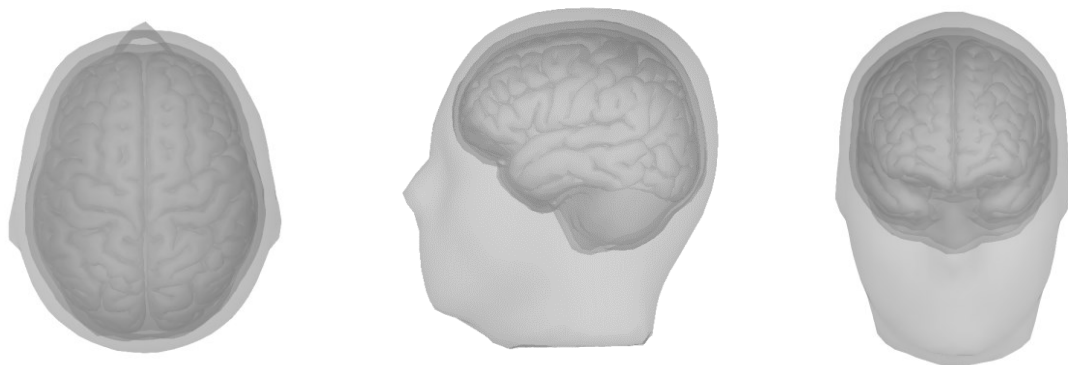


Figure 17: Default anatomy model.

2.7 Data analysis

2.7.1 Group analysis

2.7.1.1 GMFP across the entire time range of interest

TEPs can serve as a tool for assessing the overall neural activity across different cortical regions. This assessment can be accomplished by employing a metric known as the global mean field power (GMFP).

$$GMFP(t) = \sqrt{\frac{\sum_i^k (V_i(t) - V_{mean}(t))^2}{K}},$$

Where K is the number of channels, V is the voltage at channel i and t is time.

At each time point, computing GMFP involves determining the standard deviation across all electrodes. Time instances that align with the TEP peaks result in high GMFP peaks, whereas smaller TEP components yield lower GMFP peaks.

In order to have an initial measure reflecting the effects on signal amplitude induced by the application of the different preprocessing methods, we assessed the average of the GMFP over the entire range of interest from 0 to 250 ms.

To investigate statistical significance, we used a non-parametric ANOVA (Friedman's test). We also used post-hoc tests for pairwise comparisons: Durbin-Conover test and Wilcoxon's test. These tests, like all the statistical analysis in this thesis, were implemented using the jamovi software [68].

2.7.1.2 GMFP across time windows

As in previous studies, the dynamics of EEG signal after the application of a TMS pulse to the M1 cortex were assessed in three specific time epochs after the TMS pulse.

These physiological epochs are framed in three time windows:

- the *early* window, from 20 to 80 ms;
- the *middle* window, from 80 to 150 ms;
- the *late* window, from 150 to 250 ms.

As we already done with the entire range we are going to evaluate the GMFP in each time window of interest.

The same statistical tests are applied for each time window, in the same way we did for the entire time interval.

2.7.1.3 Peaks analysis

After assessing the magnitude of the GMFP over the time windows of interest, I went into more detail trying to identify the peaks of activity. In particular, I tried to define their number,

amplitudes and latencies. For the early window the research it's been focused on the P30, N45 and P60 peaks. While for the middle window we looked for the N100 peak, and for the late window for the P180 peak.

2.7.1.4 Latencies and amplitudes

Since it was not always possible to identify all the peaks of interest in the early window in the GMFP, we proceeded to the assessment of the peaks around the stimulated area, in particular on the FC3 C5 C3 C1 CP3 electrodes, by evaluating the Local Mean Field Power (LMFP). In contrast with GMFP, LMFP reflects local cortical reactivity.

Since some peaks were still not identified by all the pipelines, we applied another approach. First, considered a latency interval for each peak of interest within which we were able to find values beforehand: 27-37 ms for N30, 42-52 ms for N45, 56-68 ms for P60. Then, we did an averaging-time on Brainstorm of these intervals in the subjects (and in the pipeline) where we did not find one or more peaks. We plotted the corresponding topography and picked up the channel with the highest amplitude, along with the four neighbouring channels. We then calculated the LMFP of the identified ROI and averaged over the latency interval, obtaining a value to use as the amplitude of that specific peak that we could not find.

To evaluate possible differences in latencies, we considered the channels of the ROI and plotted the average of the five selected electrodes to look for deflections that could be associated with a peak. In this case, it was not possible to find latency values that could be informative.

We then applied a non-parametric ANOVA (Friedman's test) and a Wilcoxon test to assess possible differences in amplitudes; we did the same with the middle and the late latencies, while for the early latencies we only performed a Wilcoxon test.

2.7.1.5 Butterfly plots, topographies and source localizations

Finally, using Brainstorm, we averaged across subjects and obtained three butterfly plots summarising the effects of the three preprocessing pipelines in our population.

We also performed the average-time for all time intervals where the peaks of interest were found, in the same way as we looked for reasonable LMFP values for the missing peaks.

In particular:

- for peak P30 we selected the interval 27-37 ms,
- for peak N45 we selected the interval 42-52 ms,
- for peak P60 we selected the interval 56-68 ms,
- for peak N100 we selected the interval 94-133 ms,

- for peak P180 we selected the interval 175-229 ms.

We then plotted the topographies corresponding to these intervals to obtain a 2D representation of the voltage map on the scalp. We also calculated the corresponding source localisations to evaluate if the dynamics of the different TEP peaks in the different time windows were consistent with the topographies and, more importantly, with the physiological cortical activation. To do this, we used a default BEM model on Brainstorm and the MNE approach to obtain a current density map.

For both topographies and localisations, the potential and current values were normalised with respect to the local maximum.

2.7.2 Individual analysis

We will also see how the different pipelines affected the datasets of each individual subject. We will see how many degrees of freedom are suppressed with the application of each pipeline. We will also create butterfly plots to get a qualitative insight into how the different approaches affect the raw data. We also plot the GMFP and the LMFP, with the related peaks analysis.

For each peak identified, we also plotted the corresponding topography.

3.1 Group analysis

3.1.1 GMFP across the entire time range of interest

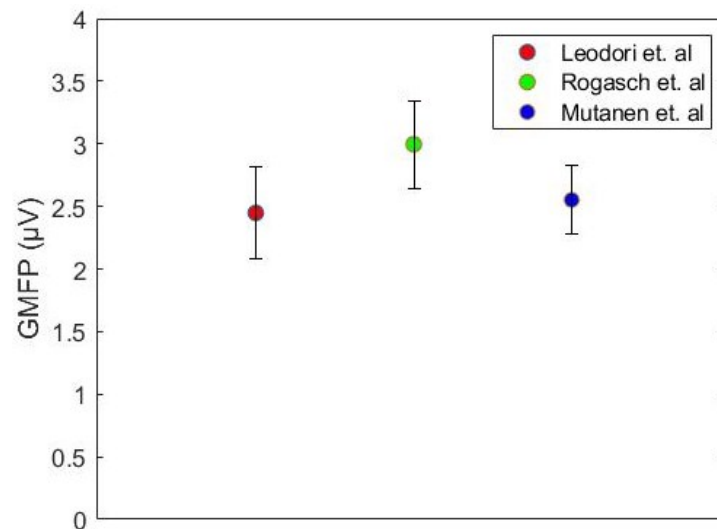


Figure 18: GMFP amplitude averaged across the entire time interval 20-250 ms. The Standard Error (SE) bar is also plotted ($SE = SD/\sqrt{n}$, where n is the number of subjects).

Table 4: GMFP global average values in μV across the entire interval with the standard deviation (SD).

Leodori et. al	Rogasch et. al	Mutanen et. al
2.45±0.822	2.99±0.78	2.55±0.61

Table 5: Statistical outcome of the GMFP for the interval 20-250 ms.

Friedman	Pairwise Comparisons (Durbin-Conover)	p	Pairwise Comparisons (Wilcoxon)	p
	$p = 0.041$	Leodori et.al – Rogasch et.al	0.096	Leodori et.al – Rogasch et.al
	Leodori et.al – Mutanen et.al	0.096	Leodori et.al – Mutanen et.al	0.625
	Rogasch et.al – Mutanen et.al	0.005	Rogasch et.al – Mutanen et.al	0.063

3.1.2 GMFP across three defined time windows

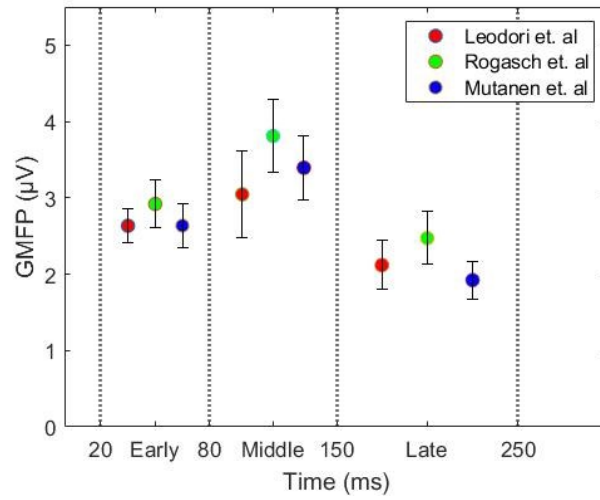


Figure 19: GMFP amplitude average for each time window of interest, with the SE bar.

Table 6: GMFP global average values in μV across each time window, the standard deviation is also indicated.

	<i>Early</i>	<i>Middle</i>	<i>Late</i>
Leodori et. al	2.63±0.51	3.05±1.28	2.12±0.72
Rogasch et. al	2.92±0.70	3.81±1.06	2.47±0.77
Mutanen et. al	2.64±0.65	3.39±0.95	1.92±0.57

Table 7: Friedman test output for each time window of interest.

Friedman	<i>Early</i>	<i>Middle</i>	<i>Late</i>
	$p = 0.247$	$p = 0.074$	$p = 0.091$

Table 8: Pairwise comparison output for each time window of interest.

<i>Early</i>	Pairwise Comparisons (Durbin-Conover)	<i>p</i>	Pairwise Comparisons (Wilcoxon)	<i>p</i>
	Leodori et.al – Rogasch et.al	0.219	Leodori et.al – Rogasch et.al	0.125
	Leodori et.al – Mutanen et.al	0.747	Leodori et.al – Mutanen et.al	1
	Rogasch et.al – Mutanen et.al	0.134	Rogasch et.al – Mutanen et.al	0.188

<i>Middle</i>	Pairwise Comparisons (Durbin-Conover)	<i>p</i>	Pairwise Comparisons (Wilcoxon)	<i>p</i>
	Leodori et.al – Rogasch et.al	0.438	Leodori et.al – Rogasch et.al	0.625
	Leodori et.al – Mutanen et.al	0.076	Leodori et.al – Mutanen et.al	0.625
	Rogasch et.al – Mutanen et.al	0.021	Rogasch et.al – Mutanen et.al	0.063

<i>Late</i>	Pairwise Comparisons (Durbin-Conover)	<i>p</i>	Pairwise Comparisons (Wilcoxon)	<i>p</i>
	Leodori et.al – Rogasch et.al	0.046	Leodori et.al – Rogasch et.al	0.125
	Leodori et.al – Mutanen et.al	1	Leodori et.al – Mutanen et.al	0.813
	Rogasch et.al – Mutanen et.al	0.046	Rogasch et.al – Mutanen et.al	0.063

3.1.3 Peaks analysis

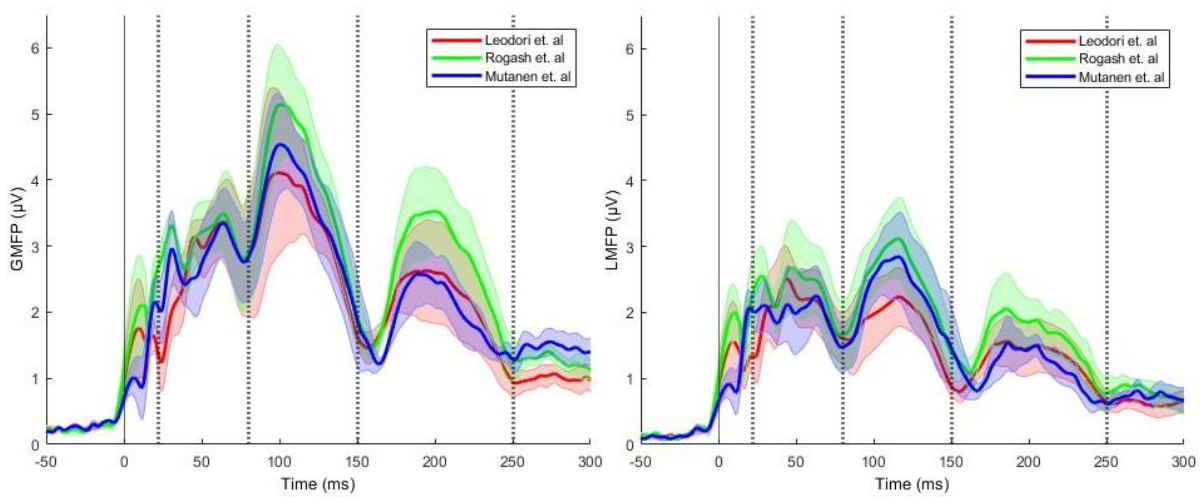


Figure 20: Average of the GMFP and LMFP values across subjects. The shaded area is the SE.

3.1.3.1 Number of peaks

Table 9: Numerosity of peaks analysis.

		Percentage of peaks found				
		<i>Early</i>			<i>Middle</i>	
Average number of peaks found		P30	N45	P60	N100	P180
Leodori et. al	4	60%	60%	100%	100%	100%
Rogash et. al	4	100%	40%	80%	100%	100%
Mutanen et. al	4	80%	60%	60%	100%	100%

3.1.3.2 Latencies and amplitudes

Table 10: Latency and amplitude analysis.

<i>LATENCY, ms</i>	<i>LMFP analysis</i>			<i>GMFP analysis</i>	
	<i>Early</i>			<i>Middle</i>	<i>Late</i>
	P30	N45	P60	N100	P180
Leodori et.al	31.67±5.03	44±1	59.75±5.56	113.60 ± 14.57	203.60 ± 21.63
Rogasch et.al	31.0±3.87	48.33±3.2	62.25±4.92	112.20 ± 9.28	203.20 ± 11.41
Mutanen et.al	30.75±3.10	44.33±2.82	61.40±5.55	112.80 ± 9.63	197 ± 8.86
<i>AMPLITUDES, μV</i>					
Leodori et.al	2.34±0.80	2.86±1.20	2.53±1.10	4.52 ± 2	2.68 ± 1.28
Rogasch et.al	2.80±0.83	3.65±1.48	2.29±1.10	5.64 ± 1.68	3.54 ± 1.40
Mutanen et.al	2.39±0.79	2.68±1.54	2.43±1.24	4.85 ± 1.50	2.70 ± 0.97

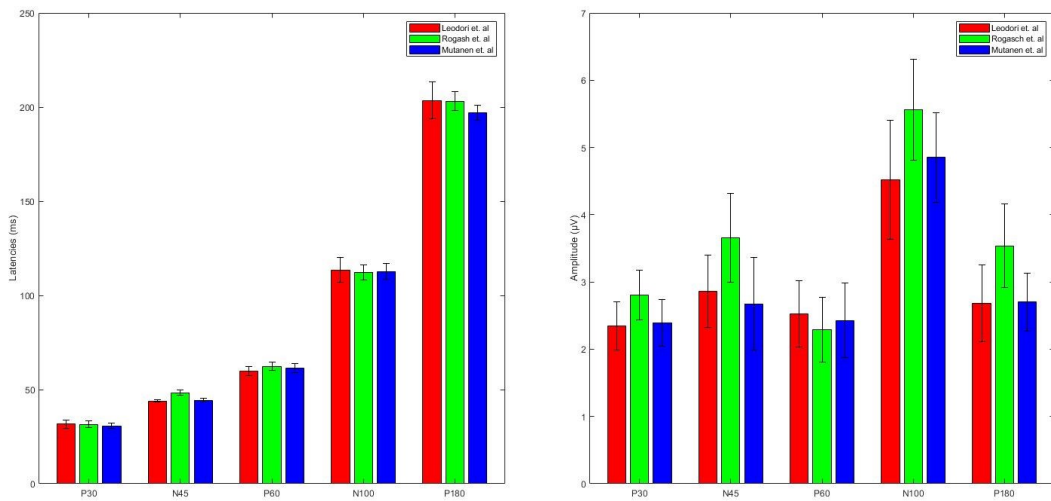


Figure 21: Latencies and amplitudes bar plots with the SE.

Table 11: Latencies statistical analysis output.

Latencies			Latencies					
Friedman (p-values)	Middle	Late	Pairwise Comparisons (Wilcoxon) (p-values)			Early	Middle	Late
	N100	P180		P30	N45	P60	N100	P180
	0.678	0.074						
			Leodori et.al – Rogasch et.al	1	0.346	1	0.855	0.786
			Leodori et.al – Mutanen et.al	0.414	0.346	0.371	1	0.313
			Rogasch et.al – Mutanen et.al	0.371	0.346	0.773	0.855	0.063

Table 12: Amplitudes statistical analysis output.

Amplitudes					
Friedman	Early			Middle	Late
	P30	N45	P60	N100	P180
	1	0.549	0.819	0.041	0.074

Amplitudes					
Pairwise Comparisons (Wilcoxon) (p-values)	Early			Middle	Late
	P30	N45	P60	N100	P180
Leodori et.al – Rogasch et.al	1	0.813	0.313	0.188	0.125
Leodori et.al – Mutanen et.al	0.625	0.813	0.625	0.625	1
Rogasch et.al – Mutanen et.al	0.813	0.188	0.813	0.063	0.063

3.1.4 Butterfly plots, topographies and source localizations

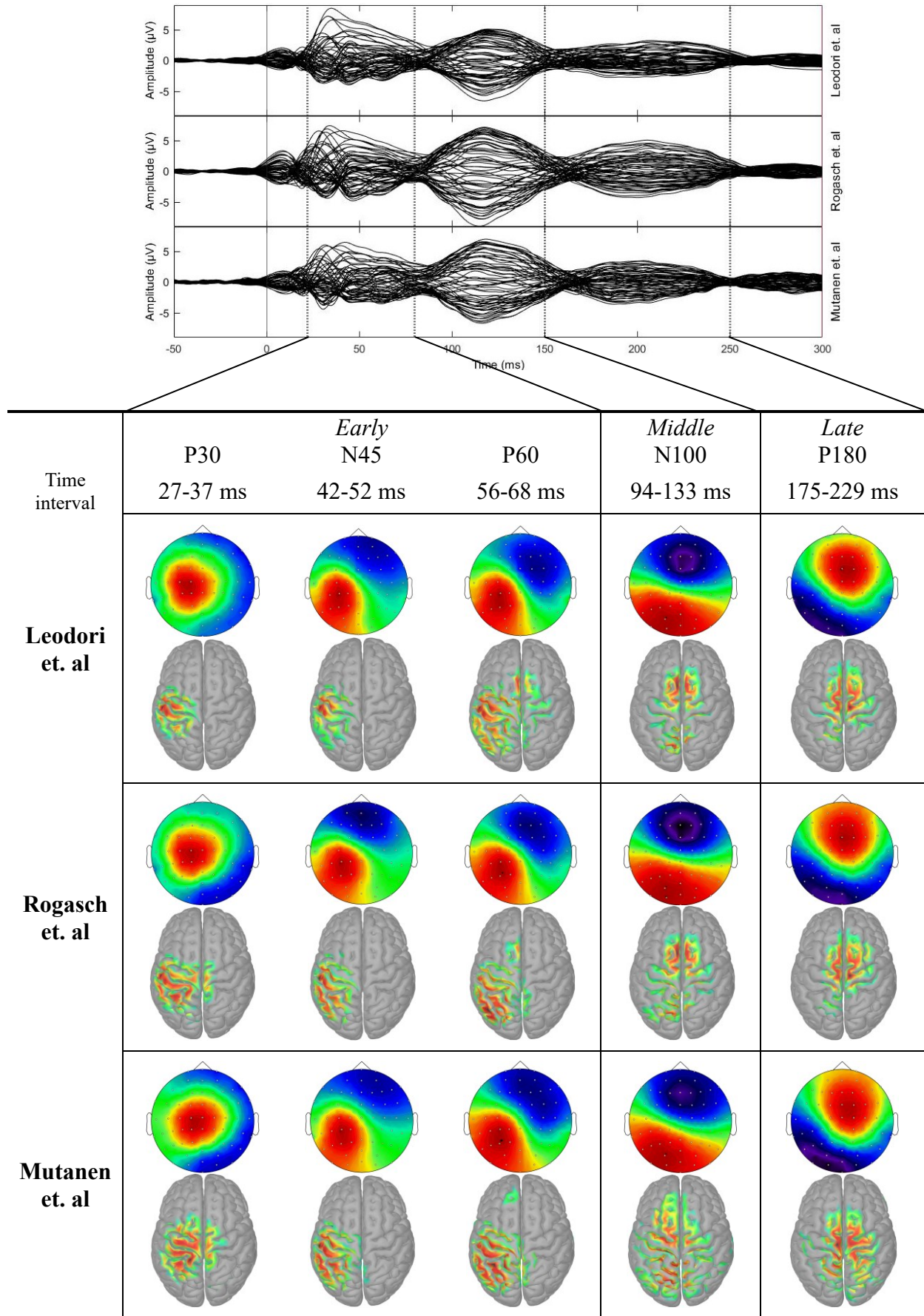


Figure 22: Butterfly plots, topographies and source localizations for each average-time interval of interest.

3.2 Individual analysis

3.2.1 Subject 01

Table 13: Degrees of freedom removed by the pipelines from Subject 01 raw data.

	1 st ICA components, variance	2 nd ICA components, variance	Bad channels	PCs SSP-SIR	Bad trials
Leodori et.al	1/62 (4.3%)	34/61 (92.34%)	-	-	0
Rogasch et. al	18/48 (5.29%)	11/30 (94.5%)	14	-	0
Mutanen et. al	5/61 (62.2%)	-	-	1	0

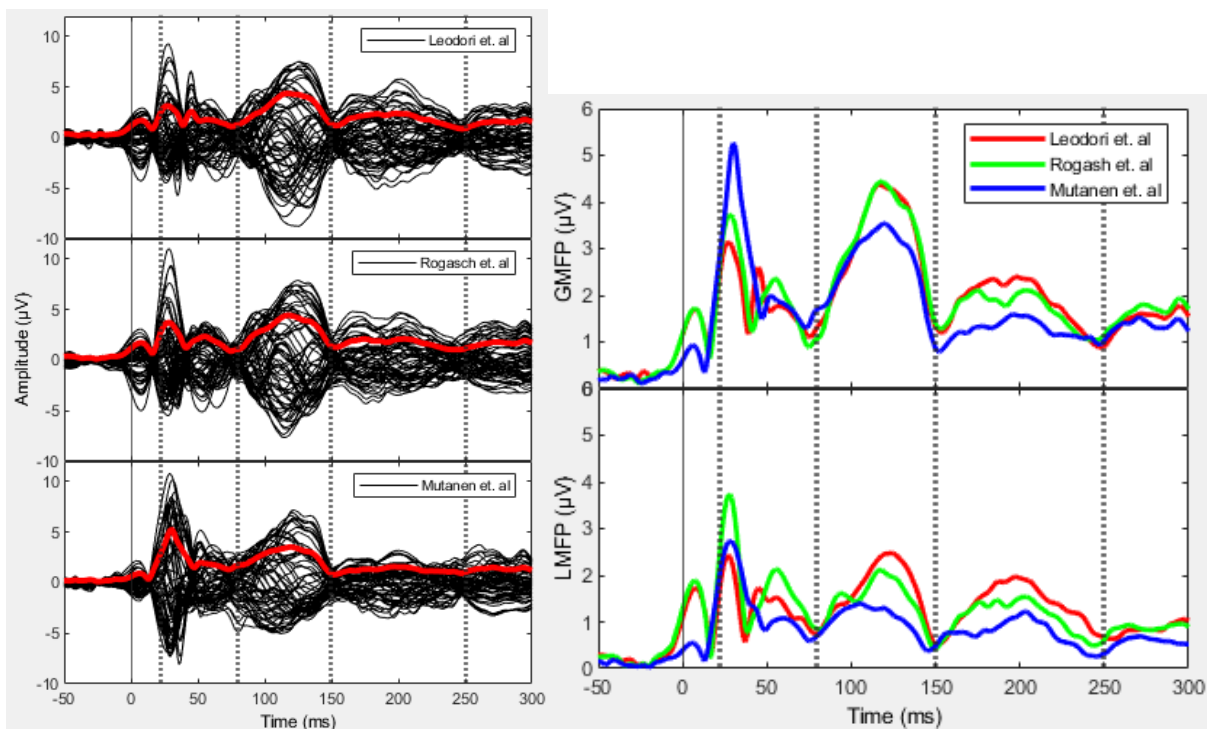
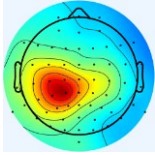
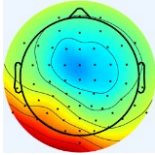
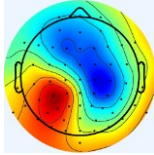
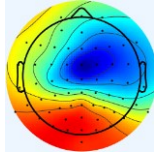
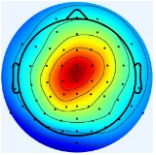
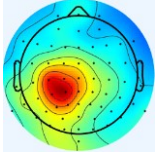
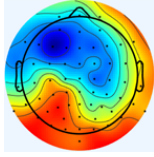
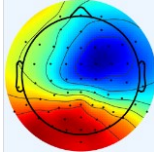
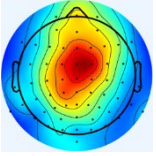
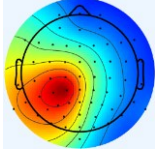
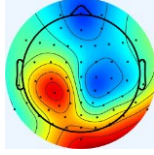
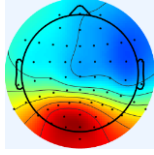
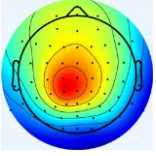


Figure 23: Butterfly plots, GMFP and LMFP.

Table 14: Peaks analysis.

	<i>LMFP analysis</i>			<i>GMFP analysis</i>	
<i>LATENCY, ms</i>	<i>Early</i>			<i>Middle</i>	<i>Late</i>
<i>ms</i>	P30	N45	P60	N100	P180
Leodori et. al	27	45	56	117	198
Rogasch et. al	28	-	56	118	204
Mutanen et. al	28	-	60	120	197
<i>AMPLITUDE, μV</i>					
Leodori et. al	2.43	1.73	1.53	4.37	2.40
Rogasch et. al	3.74	-	2.12	4.44	2.12
Mutanen et. al	2.73	-	1.08	3.54	1.59

Table 15: Topographies.

	<i>Early</i>			<i>Middle</i>	<i>Late</i>
	P30	N45	P60	N100	P180
Peak's analysis latencies (ms)	27	45	56	117	198
Leodori et. al					
Peak's analysis latencies (ms)	28		56	118	204
Rogasch et. al					
Peak's analysis latencies (ms)	28		60	120	197
Mutanen et. al					

3.2.2 Subject 02

Table 16: Degrees of freedom removed by the pipelines from Subject 02 raw data.

	1 st ICA components, variance	2 nd ICA components, variance	Bad channels	PCs SSP-SIR	Bad trials
Leodori et.al	30/62 (42.88%)	13/32 (43.09%)	-	-	12
Rogasch et. al	24/56 (18.63%)	20/32 (66.53%)	6	-	11
Mutanen et. al	4/61 (8.98%)	-	-	1	7

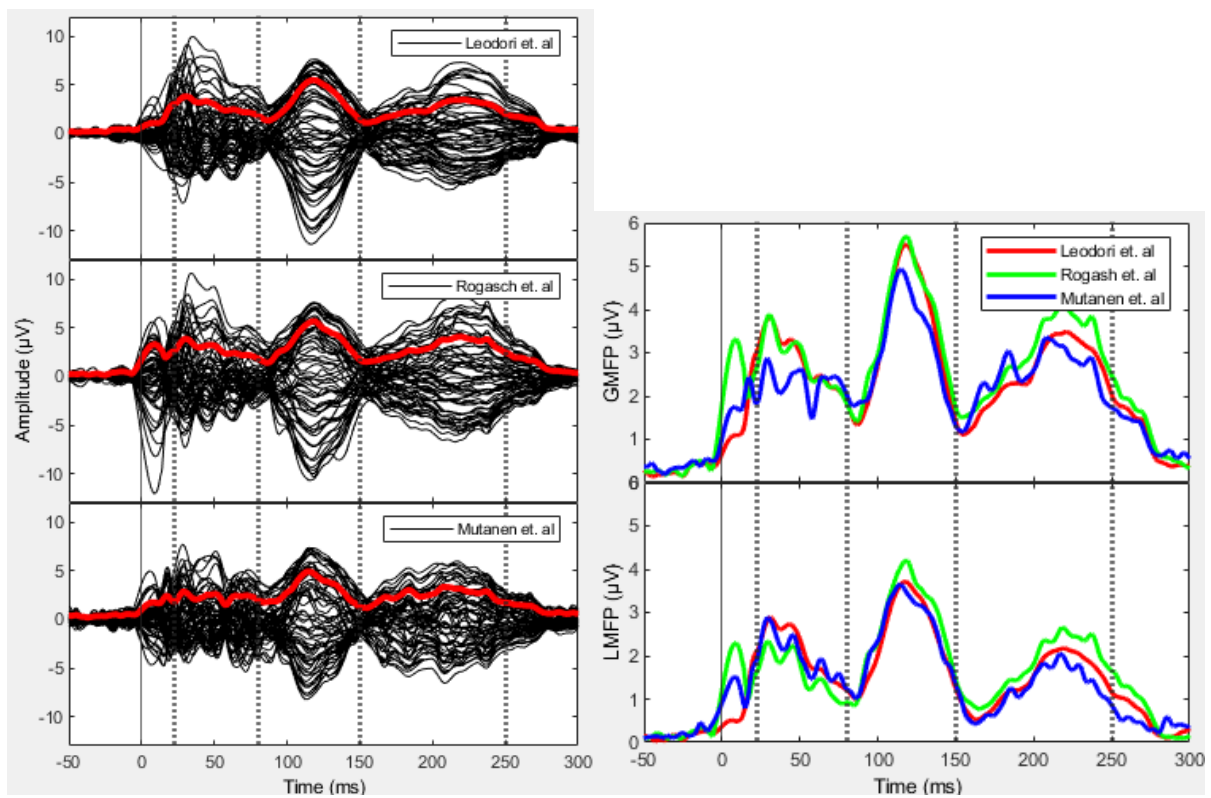
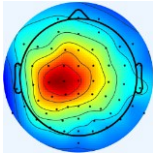
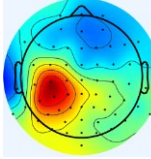
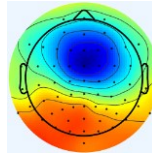
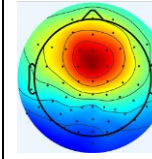
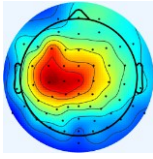
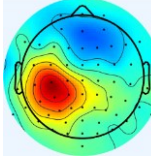
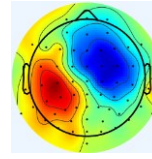
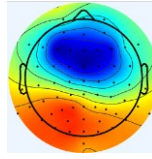
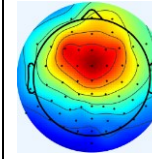
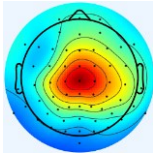
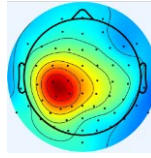
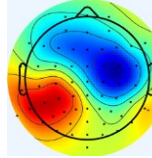
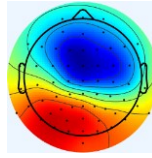
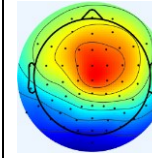


Figure 24: Butterfly plots, GMFP and LMFP.

Table 17: Peaks analysis.

	<i>LMFP analysis</i>			<i>GMFP analysis</i>	
<i>LATENCY, ms</i>	<i>Early</i>			<i>Middle</i>	<i>Late</i>
<i>ms</i>	P30	N45	P60	N100	P180
Leodori et. al	31	43	-	118	221
Rogasch et. al	30	46	63	118	219
Mutanen et. al	29	45	64	115	208
<i>AMPLITUDE, μV</i>					
Leodori et. al	2.89	2.73	-	5.50	3.48
Rogasch et. al	2.33	2.24	1.47	5.69	4.11
Mutanen et. al	2.88	2.49	1.93	4.92	3.35

Table 18: Topographies.

	P30	<i>Early</i> N45	P60	<i>Middle</i> N100	<i>Late</i> P180
Peak's analysis latencies (ms)	31	43		118	221
Leodori et. al					
Peak's analysis latencies (ms)	30	46	63	118	219
Rogasch e. al					
Peak's analysis latencies (ms)	29	45	64	115	208
Mutanen et. al					

3.2.3 Subject 03

Table 19: Degrees of freedom removed by the pipelines from Subject 03 raw data.

	1 st ICA components, variance	2 nd ICA components, variance	Bad channels	PCs SSP-SIR	Bad trials
Leodori et.al	20/62 (18.18%)	15/42 (79.22%)	-	-	1
Rogasch et. al	15/57 (6.73%)	14/42 (65.16%)	5	-	2
Mutanen et. al	3/61 (7.83%)	-	-	1	0

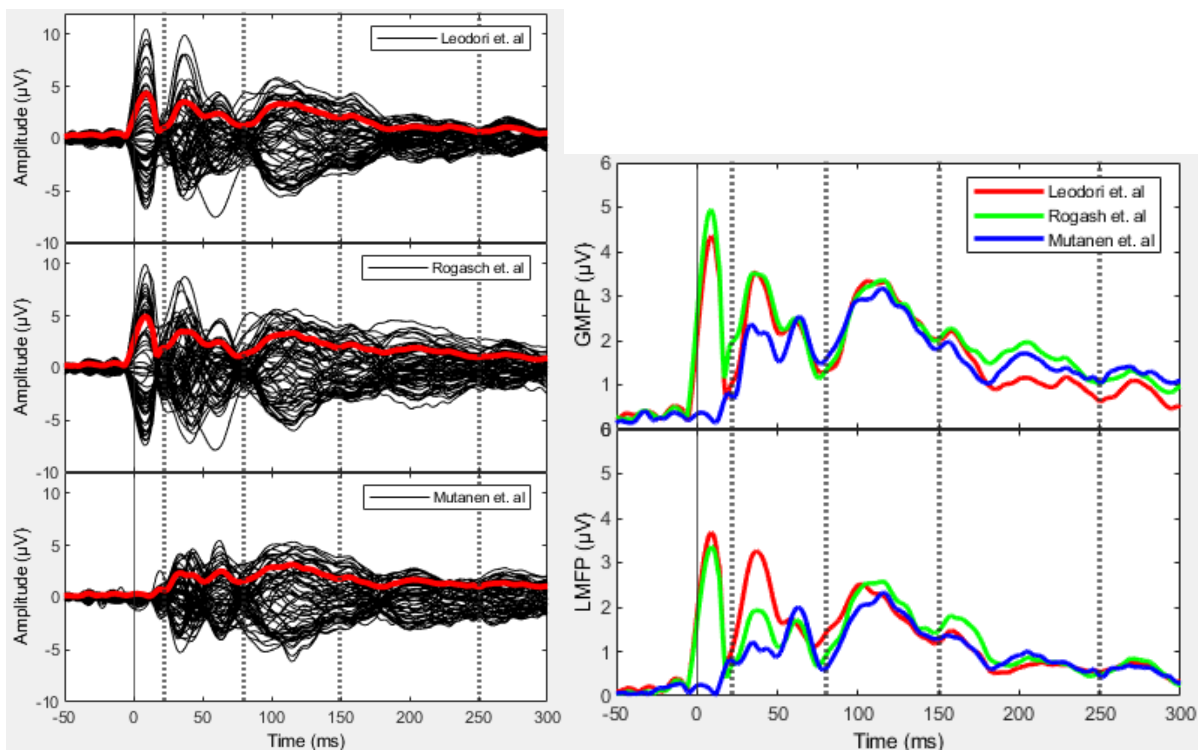
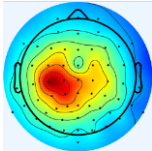
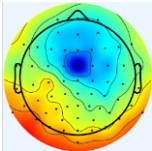
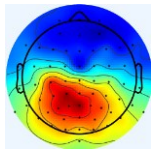
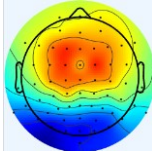
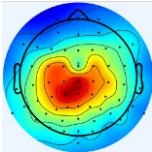
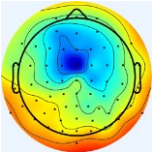
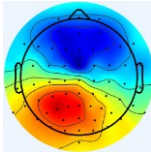
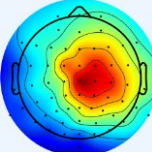
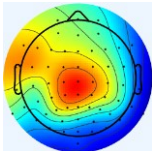
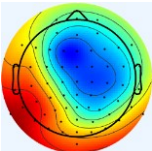
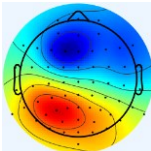
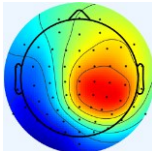


Figure 25: Butterfly plots, GMFP and LMFP.

Table 20: Peaks analysis.

	<i>LMFP analysis</i>			<i>GMFP analysis</i>	
<i>LATENCY, ms</i>	<i>Early</i>			<i>Middle</i>	<i>Late</i>
<i>ms</i>	P30	N45	P60	N100	P180
Leodori et. al	37	-	58	106	229
Rogasch et. al	37	-	62	116	205
Mutanen et. al	35	42	62	115	203
<i>AMPLITUDE, μV</i>					
Leodori et. al	3.26	-	1.73	3.34	1.18
Rogasch et. al	1.92	-	1.70	3.36	1.96
Mutanen et. al	1.22	1.24	2.16	3.17	1.71

Table 21: Topographies

	P30	<i>Early</i> N45	P60	<i>Middle</i> N100	<i>Late</i> P180
Peak's analysis latencies (ms)	37		58	106	229
Leodori et. al					
Peak's analysis latencies (ms)	35		62	116	205
Rogasch et. al					
Peak's analysis latencies (ms)	35		62	115	203
Mutanen et. al					

3.2.4 Subject 04

Table 22: Degrees of freedom removed by the pipelines from Subject 04 raw data.

	1 st ICA components, variance	2 nd ICA components, variance	Bad channels	PCs SSP-SIR	Bad trials
Leodori et.al	31/62 (9.17%)	15/31 (97%)	-	-	7
Rogasch et. al	20/41 (0.71%)	10/21 (91.94%)	21	-	4
Mutanen et. al	2/61 (0.02%)	-	-	1	2

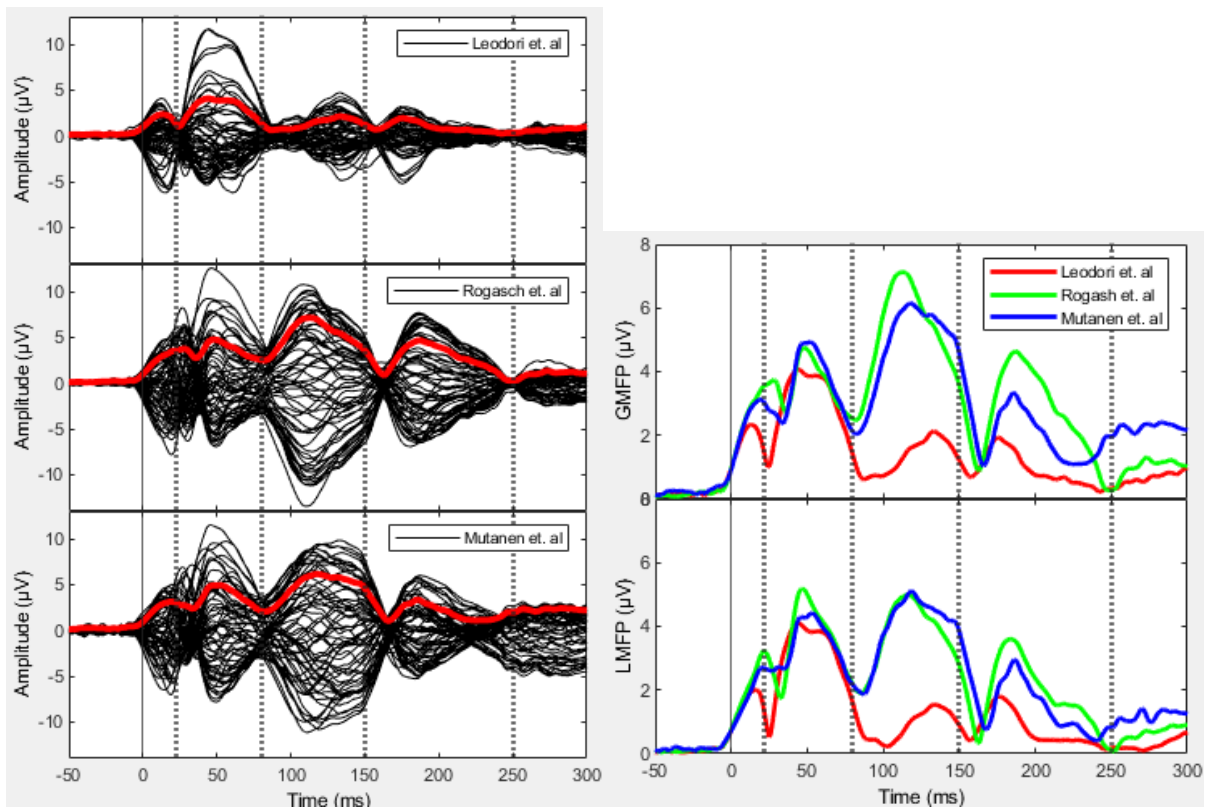
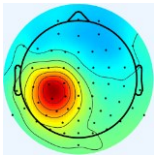
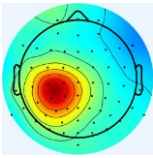
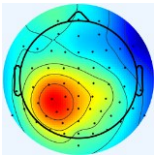
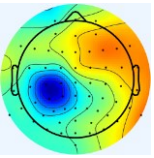
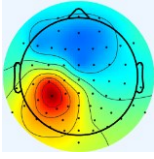
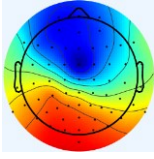
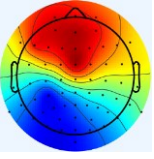
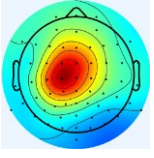
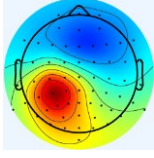
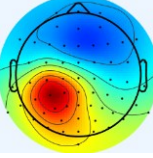
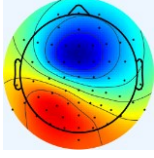
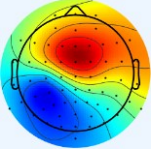


Figure 26: Butterfly plots, GMFP and LMFP.

Table 23: Peaks analysis.

	<i>LMFP analysis</i>			<i>GMFP analysis</i>	
<i>LATENCY, ms</i>	<i>Early</i>			<i>Middle</i>	<i>Late</i>
<i>ms</i>	P30	N45	P60	N100	P180
Leodori et. al	-	44	57	133	175
Rogasch et. al	-	47	-	113	187
Mutanen et. al	31	46	53	118	186
<i>AMPLITUDE, μV</i>					
Leodori et. al	-	4.12	3.85	2.13	1.93
Rogasch et. al	-	5.19	-	7.12	4.64
Mutanen et. al	2.73	4.30	4.42	6.15	3.34

Table 24: Topographies.

	P30	<i>Early</i> N45	P60	<i>Middle</i> N100	<i>Late</i> P180
Peak's analysis latencies (ms)		44	57	133	175
Leodori et. al					
Peak's analysis latencies (ms)		47		113	187
Rogasch et.al					
Peak's analysis latencies (ms)	31	46	53	118	186
Mutanen et. al					

3.2.5 Subject 05

Table 25: Degrees of freedom removed by the pipelines from Subject 05 raw data.

	1 st ICA components, variance	2 nd ICA components, variance	Bad channels	PCs SSP-SIR	Bad trials
Leodori et.al	29/62 (47.61%)	12/33 (76.41%)	-	-	2
Rogasch et. al	16/44 (16.76%)	8/28 (70.87%)	18	-	2
Mutanen et. al	4/60 (11.46%)	-	-	2	0

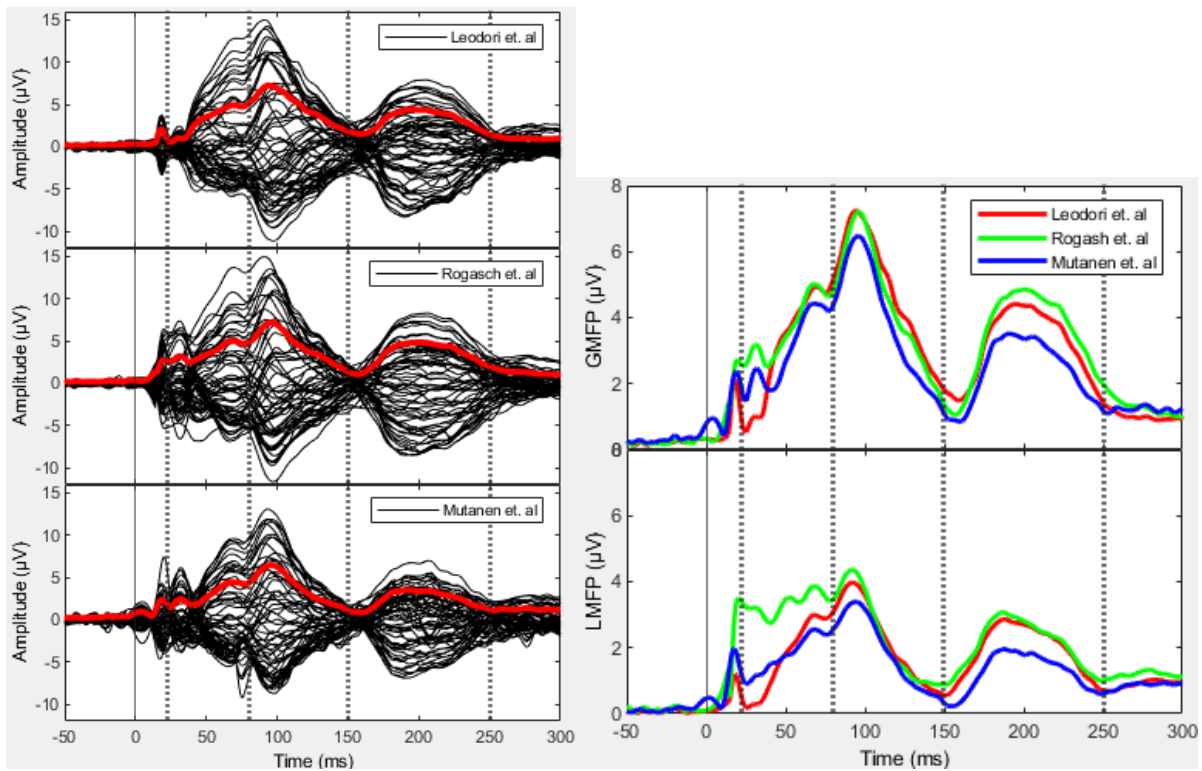
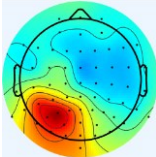
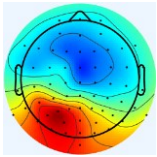
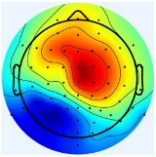
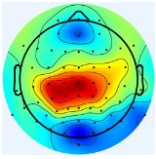
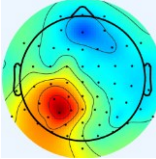
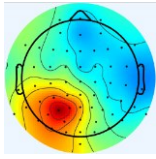
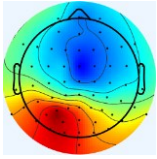
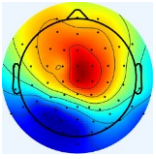
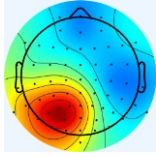
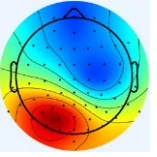
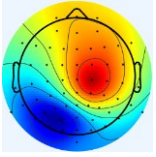


Figure 27: Butterfly plots, GMFP and LMFP.

Table 26: Peaks analysis.

	<i>LMFP analysis</i>			<i>GMFP analysis</i>	
<i>LATENCY, ms</i>	<i>Early</i>			<i>Middle</i>	<i>Late</i>
<i>ms</i>	P30	N45	P60	N100	P180
Leodori et. al	-	-	68	94	195
Rogasch et. al	31	52	68	96	201
Mutanen et. al	-	-	68	96	191
<i>AMPLITUDE, μV</i>					
Leodori et. al	-	-	3.00	7.25	4.42
Rogasch et. al	3.22	3.53	3.87	7.21	4.86
Mutanen et. al	-	-	2.56	6.48	3.51

Table 27: Topographies.

	<i>Early</i>			<i>Middle</i>	<i>Late</i>
	P30	N45	P60	N100	P180
Peak's analysis latencies (ms)			68	94	195
Leodori et. al					
Peak's analysis latencies (ms)	31	52	68	96	201
Rogasch et. al					
Peak's analysis latencies (ms)			68	96	191
Mutanen et. al					

Discussion

We compared the effects of different preprocessing pipelines (Leodori et al., Rogasch et al. and Mutanen et al.) on TEPs recorded after the stimulation of M1 in five healthy subjects and we observed considerable variability in the effects produced on different signal characteristics.

To analyse these effects, we assessed the amplitude of the GMFP averaged over the entire time interval of interest, and we observed that the pipeline of Rogasch et al. showed, on average, higher values thanLeodori et al. and Mutanen et al. which, conversely, produced signals with very similar mean amplitudes. Furthermore, the pipeline of Mutanen et al. was characterised by less variability, suggesting a greater stability in its approach across subjects. The statistical results also showed significant differences between Rogasch et al. and Mutanen et al., as expected, as these two pipelines are the most dissimilar.

Then, the average amplitude of GMFP was assessed in three different time windows. When TEPs were analysed with the pipeline by Rogasch et al. we observed the highest GMFP amplitude values in all three windows, whileLeodori et. al and Mutanen et. al showed lower and more similar values. Interestingly, despite slight differences in the steps, the pipelines by Rogasch et al. andLeodori et al. produced results with different amplitudes.

In the early time window, the three approaches were similar on average, but showed significant variations. Notably,Leodori et al. stands out with less variability with respect to the other two, while Rogasch et al. is characterised by a higher standard error (SE).

Among the three time windows considered, the middle window showed the greatest variability, both between subjects and between methods. The results of the statistical analysis suggest a trend towards significance in the differences between the middle and late windows, due to the disparities between the approaches of Rogasch et al. and Mutanen et al. Since bothLeodori et al. and Rogasch et al. differ significantly from Mutanen et al., these data confirm thatLeodori et al. and Rogasch et al. adopt a very similar approach and apply similar corrections to the signal.

When considering separately the different time windows, we did not observe statistically significant differences in the average number of peaks identified. Interestingly, the peaks N100 and P180 in the middle and late windows were always identified, regardless of the subject or pipeline used. These peaks are the most reliable and stable in TEPs, as also confirmed in the literature [1]. Our results are in line with these findings, as the later latencies appear to be the most robust.

It is important, however, to remember that the later components could be a combination of the direct effect of TMS stimulation and auditory and other sensory-evoked responses.

With regard to peaks in the early window, we observed greater variability in the identification of peaks. Our results suggest that Rogasch et al. pipeline is more accurate in detecting the P30 peak than the other two. However, peak N45 was less accurately detected in Rogasch et al. pipeline than in the other two, but similarly between Leodori et. al and Rogasch et. al. Finally, it appears that the Leodori et al. pipeline is the most effective in detecting the P60 peak.

The latencies of the detected peaks show different patterns of variability, with the peaks after the first 100 ms showing more variation than the earlier peaks, which remain closer to the average. Variability between pipelines is generally negligible on average for latencies, statistical tests however show us significant differences in latency for peak P180 that are explained by differences between Rogasch et al. and Mutanen et al.

Peaks amplitudes show greater variability between subjects than latencies, resulting in a trend of statistical significance for peaks N100 and P180, mainly due to differences between Rogasch et al. and Mutanen et al.

All this further underlines the importance of the choice of preprocessing pipeline on TEPs, especially at early latencies, with an impact on their reproducibility. Unfortunately, early TEP components are often contaminated with large artefacts, such as TMS pulse artefact, muscle and decay artefacts, which compromise the SNR and make this part of the signal particularly difficult to evaluate. Consequently, the selection of the right preprocessing pipeline is crucial for improving signal quality.

It can be seen that although two of the three pipelines (Leodori et al. and Rogasch et al.) are very similar and have only a few variations in the processing steps, they have non-negligible differences in the analysis outcome.

The three approaches also differ in the number of bad trials removed. In fact, the Mutanen et al. pipeline, which uses specific and automated methods (SOUND and SSP-SIR) to remove artifacts the signal before trial rejection, systematically removed fewer trials than the other two pipelines.

Another difference that must be outlined is the level of automatism between the different approaches. The rejection of the independent artefactual components in the ICA rounds is indeed supervised by the user and may differ across users. However, in the pipelineLeodori et al. the rejection of bad electrodes is performed automatically by the TESA plugin. The level of automatism in Mutanen et al.'s pipeline is the highest, in fact the SOUND and SSP-SIR work essentially autonomously. Of note, higher level of automatism would be preferable to reduced operator-based biases and to increase the efficiency of the preprocessing.

Although ICA has long been used as a method for feature selection and is recognised as a valid method in EEG analysis, it may not be the most suitable tool for separating brain signal from artefacts in TEPs; indeed, this method assumes non-dependence between the components. In TMS-EEG, however, this is not always true as many artefacts are time-locked to the TMS pulse [1].

Furthermore, the application of a specific pipeline should be also guided by the nature of the available data. In some cases, it may be tempting to use the same framework, but artefacts may vary considerably from one recording to another. For example, in some recordings there may be numerous corrupted channels due to the low quality of recordings, and removing these channels could significantly reduce degrees of freedom. In other situations, there may be more artefacts due to movement, especially in particularly agitated subjects.

Despite the differences between the methods, we observed that the comparison of topographies and localisation sources are consistent and reliable for all latencies of interest. It is important to note, that for all visualisations the current and potential values were normalised to the local maximum, as it is assumed that signal amplitude does not determine the quality of a pipeline. What is really relevant is to be able to accurately describe the TEPs dynamics, which provide the most valuable information on the underlying neural processes.

This could be misleading when exchanging data between research groups using different scales, in which case the data may not be reproducible.

5

Conclusions

The main issue in identifying an optimal pipeline is the lack of knowledge of the actual signal we intend to reconstruct. It is also crucial to emphasise that we only examined three different pipelines in our study, however, several other preprocessing pipelines have been proposed, each with distinct characteristics. Disparities between these pipelines are a critical issue in the analysis of TEPs and could be mitigated when results are based on a comparison of two conditions processed using the same approach.

Another crucial aspect is the improvement of EEG recording by minimizing the artifactual components, in order to optimise the signal-to-noise ratio. This effort may lead to more robust results that are less influenced by pipeline selection.

Furthermore, a possible strategy that could assist and contribute to the characterisation of TEP components is the use of different methods on the same dataset, known as “multiverse analysis” [1], [69]. This approach could be useful to control the variability inherent to different methods.

The main limitation of the present study is the small sample size of the enrolled subjects, which may have affected the reliability of statistical analyses. Nevertheless, this research provides several interesting clues even in this small population, that will be further explored in future studies considering a larger population of healthy subjects.

References

- [1] G. Bertazzoli *et al.*, ‘The impact of artifact removal approaches on TMS–EEG signal’, *NeuroImage*, vol. 239, p. 118272, Oct. 2021, doi: 10.1016/j.neuroimage.2021.118272.
- [2] R. J. Ilmoniemi and D. Kičić, ‘Methodology for Combined TMS and EEG’, *Brain Topogr*, vol. 22, no. 4, pp. 233–248, Jan. 2010, doi: 10.1007/s10548-009-0123-4.
- [3] S. Komssi and S. Kähkönen, ‘The novelty value of the combined use of electroencephalography and transcranial magnetic stimulation for neuroscience research’, *Brain Research Reviews*, vol. 52, no. 1, pp. 183–192, Aug. 2006, doi: 10.1016/j.brainresrev.2006.01.008.
- [4] D. Veniero, M. Bortoletto, and C. Miniussi, ‘Cortical modulation of short-latency TMS-evoked potentials’, *Front. Hum. Neurosci.*, vol. 6, 2013, doi: 10.3389/fnhum.2012.00352.
- [5] S. Tremblay *et al.*, ‘Clinical utility and prospective of TMS–EEG’, *Clinical Neurophysiology*, vol. 130, no. 5, pp. 802–844, May 2019, doi: 10.1016/j.clinph.2019.01.001.
- [6] M. Rosanova, S. Casarotto, A. Pigorini, P. Canali, A. G. Casali, and M. Massimini, ‘Combining Transcranial Magnetic Stimulation with Electroencephalography to Study Human Cortical Excitability and Effective Connectivity’, in *Neuronal Network Analysis*, vol. 67, T. Fellin and M. Halassa, Eds., in *Neuromethods*, vol. 67. , Totowa, NJ: Humana Press, 2011, pp. 435–457. doi: 10.1007/7657_2011_15.
- [7] C. Bagattini *et al.*, ‘Predicting Alzheimer’s disease severity by means of TMS–EEG coregistration’, *Neurobiology of Aging*, vol. 80, pp. 38–45, Aug. 2019, doi: 10.1016/j.neurobiolaging.2019.04.008.
- [8] L. B. Mokkink *et al.*, ‘The COSMIN study reached international consensus on taxonomy, terminology, and definitions of measurement properties for health-related patient-reported outcomes’, *Journal of Clinical Epidemiology*, vol. 63, no. 7, pp. 737–745, Jul. 2010, doi: 10.1016/j.jclinepi.2010.02.006.
- [9] L.-D. Beaulieu, V. H. Flaman, H. Massé-Alarie, and C. Schneider, ‘Reliability and minimal detectable change of transcranial magnetic stimulation outcomes in healthy adults: A systematic review’, *Brain Stimulation*, vol. 10, no. 2, pp. 196–213, Mar. 2017, doi: 10.1016/j.brs.2016.12.008.
- [10] S. Casarotto *et al.*, ‘EEG Responses to TMS Are Sensitive to Changes in the Perturbation Parameters and Repeatable over Time’, *PLoS ONE*, vol. 5, no. 4, p. e10281, Apr. 2010, doi: 10.1371/journal.pone.0010281.

- [11] P. Lioumis, D. Kičić, P. Savolainen, J. P. Mäkelä, and S. Kähkönen, ‘Reproducibility of TMS-Evoked EEG responses’, *Hum. Brain Mapp.*, vol. 30, no. 4, pp. 1387–1396, Apr. 2009, doi: 10.1002/hbm.20608.
- [12] L. J. Kerwin, C. J. Keller, W. Wu, M. Narayan, and A. Etkin, ‘Test-retest reliability of transcranial magnetic stimulation EEG evoked potentials’, *Brain Stimulation*, vol. 11, no. 3, pp. 536–544, May 2018, doi: 10.1016/j.brs.2017.12.010.
- [13] R. A. Ozdemir *et al.*, ‘Individualized perturbation of the human connectome reveals reproducible biomarkers of network dynamics relevant to cognition’, *Proc. Natl. Acad. Sci. U.S.A.*, vol. 117, no. 14, pp. 8115–8125, Apr. 2020, doi: 10.1073/pnas.1911240117.
- [14] N. C. Rogasch, M. Biabani, and T. P. Mutanen, ‘Designing and comparing cleaning pipelines for TMS-EEG data: A theoretical overview and practical example’, *Journal of Neuroscience Methods*, vol. 371, p. 109494, Apr. 2022, doi: 10.1016/j.jneumeth.2022.109494.
- [15] G. Leodori *et al.*, ‘The effect of stimulation frequency on transcranial evoked potentials’, *Translational Neuroscience*, vol. 13, no. 1, pp. 211–217, Aug. 2022, doi: 10.1515/tnsci-2022-0235.
- [16] N. C. Rogasch *et al.*, ‘Analysing concurrent transcranial magnetic stimulation and electroencephalographic data: A review and introduction to the open-source TESA software’, *NeuroImage*, vol. 147, pp. 934–951, Feb. 2017, doi: 10.1016/j.neuroimage.2016.10.031.
- [17] T. P. Mutanen, J. Metsomaa, S. Liljander, and R. J. Ilmoniemi, ‘Automatic and robust noise suppression in EEG and MEG: The SOUND algorithm’, *NeuroImage*, vol. 166, pp. 135–151, Feb. 2018, doi: 10.1016/j.neuroimage.2017.10.021.
- [18] T. P. Mutanen, M. Kukkonen, J. O. Nieminen, M. Stenroos, J. Sarvas, and R. J. Ilmoniemi, ‘Recovering TMS-evoked EEG responses masked by muscle artifacts’, *NeuroImage*, vol. 139, pp. 157–166, Oct. 2016, doi: 10.1016/j.neuroimage.2016.05.028.
- [19] J. C. Hernandez-Pavon *et al.*, ‘TMS combined with EEG: Recommendations and open issues for data collection and analysis’, *Brain Stimulation*, vol. 16, no. 2, pp. 567–593, Mar. 2023, doi: 10.1016/j.brs.2023.02.009.
- [20] P. M. Rossini *et al.*, ‘Non-invasive electrical and magnetic stimulation of the brain, spinal cord, roots and peripheral nerves: Basic principles and procedures for routine clinical and research application. An updated report from an I.F.C.N. Committee’, *Clinical Neurophysiology*, vol. 126, no. 6, pp. 1071–1107, Jun. 2015, doi: 10.1016/j.clinph.2015.02.001.

- [21] A. Suppa, F. Ascii, and A. Guerra, ‘Transcranial magnetic stimulation as a tool to induce and explore plasticity in humans’, in *Handbook of Clinical Neurology*, vol. 184, Elsevier, 2022, pp. 73–89. doi: 10.1016/B978-0-12-819410-2.00005-9.
- [22] S. Ueno and M. Sekino, ‘Figure-Eight Coils for Magnetic Stimulation: From Focal Stimulation to Deep Stimulation’, *Front. Hum. Neurosci.*, vol. 15, p. 805971, Dec. 2021, doi: 10.3389/fnhum.2021.805971.
- [23] G. Corniani, ‘Classification of EEG and fNIRS signals from Completely Locked-in State Patients for a Brain-Computer Interface communication system’, Università degli studi di Padova, 2018. [Online]. Available: <https://hdl.handle.net/20.500.12608/24540>
- [24] M. F. Bear, Connors, and Paradiso, *Neuroscience: Exploring the Brain*. 2001.
- [25] R. K. Laurens, ‘File:EEG 10-10 system with additional information.svg’, Jan. 2021. [Online]. Available: [https://en.m.wikipedia.org/wiki/10%E2%80%9310_system_\(EEG\)](https://en.m.wikipedia.org/wiki/10%E2%80%9310_system_(EEG))
- [26] C. Miniussi and G. Thut, ‘Combining TMS and EEG Offers New Prospects in Cognitive Neuroscience’, *Brain Topogr*, vol. 22, no. 4, pp. 249–256, Jan. 2010, doi: 10.1007/s10548-009-0083-8.
- [27] G. Varone *et al.*, ‘Real-Time Artifacts Reduction during TMS-EEG Co-Registration: A Comprehensive Review on Technologies and Procedures’, *Sensors*, vol. 21, no. 2, p. 637, Jan. 2021, doi: 10.3390/s21020637.
- [28] R. J. Ilmoniemi *et al.*, ‘Dealing with artifacts in TMS-evoked EEG’, in *2015 37th Annual International Conference of the IEEE Engineering in Medicine and Biology Society (EMBC)*, Milan: IEEE, Aug. 2015, pp. 230–233. doi: 10.1109/EMBC.2015.7318342.
- [29] S. Casarotto *et al.*, ‘The rt-TEP tool: real-time visualization of TMS-Evoked Potentials to maximize cortical activation and minimize artifacts’, *Journal of Neuroscience Methods*, vol. 370, p. 109486, Mar. 2022, doi: 10.1016/j.jneumeth.2022.109486.
- [30] D. Freche, J. Naim-Feil, A. Peled, N. Levit-Binnun, and E. Moses, ‘A quantitative physical model of the TMS-induced discharge artifacts in EEG’, *PLoS Comput Biol*, vol. 14, no. 7, p. e1006177, Jul. 2018, doi: 10.1371/journal.pcbi.1006177.
- [31] D. P. Burbank and J. G. Webster, ‘Reducing skin potential motion artefact by skin abrasion’, *Med. Biol. Eng. Comput.*, vol. 16, no. 1, pp. 31–38, Jan. 1978, doi: 10.1007/BF02442929.
- [32] J. Virtanen, J. Ruohonen, R. Näätänen, and R. J. Ilmoniemi, ‘Instrumentation for the measurement of electric brain responses to transcranial magnetic stimulation’, *Med. Biol. Eng. Comput.*, vol. 37, no. 3, pp. 322–326, May 1999, doi: 10.1007/BF02513307.

- [33] B. Li *et al.*, ‘Lifting the veil on the dynamics of neuronal activities evoked by transcranial magnetic stimulation’, *eLife*, vol. 6, p. e30552, Nov. 2017, doi: 10.7554/eLife.30552.
- [34] H. D. Talhouet and J. G. Webster, ‘The origin of skin-stretch-caused motion artifacts under electrodes’, *Physiol. Meas.*, vol. 17, no. 2, pp. 81–93, May 1996, doi: 10.1088/0967-3334/17/2/003.
- [35] K. L. Ruddy, D. G. Woolley, D. Mantini, J. H. Balsters, N. Enz, and N. Wenderoth, ‘Improving the quality of combined EEG-TMS neural recordings: Introducing the coil spacer’, *Journal of Neuroscience Methods*, vol. 294, pp. 34–39, Jan. 2018, doi: 10.1016/j.jneumeth.2017.11.001.
- [36] P. Berg and M. Scherg, ‘Dipole models of eye movements and blinks’, *Electroencephalography and Clinical Neurophysiology*, vol. 79, no. 1, pp. 36–44, Jul. 1991, doi: 10.1016/0013-4694(91)90154-V.
- [37] O. G. Lins, T. W. Picton, P. Berg, and M. Scherg, ‘Ocular artifacts in recording EEGs and event-related potentials II: Source dipoles and source components’, *Brain Topogr*, vol. 6, no. 1, pp. 65–78, Sep. 1993, doi: 10.1007/BF01234128.
- [38] T. Mutanen, H. Mäki, and R. J. Ilmoniemi, ‘The Effect of Stimulus Parameters on TMS–EEG Muscle Artifacts’, *Brain Stimulation*, vol. 6, no. 3, pp. 371–376, May 2013, doi: 10.1016/j.brs.2012.07.005.
- [39] R. J. Korhonen, J. C. Hernandez-Pavon, J. Metsomaa, H. Mäki, R. J. Ilmoniemi, and J. Sarvas, ‘Removal of large muscle artifacts from transcranial magnetic stimulation-evoked EEG by independent component analysis’, *Med Biol Eng Comput*, vol. 49, no. 4, pp. 397–407, Apr. 2011, doi: 10.1007/s11517-011-0748-9.
- [40] T. Paus, P. K. Sipila, and A. P. Strafella, ‘Synchronization of Neuronal Activity in the Human Primary Motor Cortex by Transcranial Magnetic Stimulation: An EEG Study’, *Journal of Neurophysiology*, vol. 86, no. 4, pp. 1983–1990, Oct. 2001, doi: 10.1152/jn.2001.86.4.1983.
- [41] B. H. Friedman and J. F. Thayer, ‘Facial muscle activity and EEG recordings: redundancy analysis’, *Electroencephalography and Clinical Neurophysiology*, vol. 79, no. 5, pp. 358–360, Nov. 1991, doi: 10.1016/0013-4694(91)90200-N.
- [42] N. C. Rogasch, R. H. Thomson, Z. J. Daskalakis, and P. B. Fitzgerald, ‘Short-Latency Artifacts Associated with Concurrent TMS–EEG’, *Brain Stimulation*, vol. 6, no. 6, pp. 868–876, Nov. 2013, doi: 10.1016/j.brs.2013.04.004.

- [43] J. C. Hernandez-Pavon *et al.*, ‘Uncovering neural independent components from highly artifactual TMS-evoked EEG data’, *Journal of Neuroscience Methods*, vol. 209, no. 1, pp. 144–157, Jul. 2012, doi: 10.1016/j.jneumeth.2012.05.029.
- [44] I. Rejer and P. Górski, ‘Independent Component Analysis for EEG Data Preprocessing - Algorithms Comparison’, in *Computer Information Systems and Industrial Management*, vol. 8104, K. Saeed, R. Chaki, A. Cortesi, and S. Wierzchoń, Eds., in Lecture Notes in Computer Science, vol. 8104. , Berlin, Heidelberg: Springer Berlin Heidelberg, 2013, pp. 108–119. doi: 10.1007/978-3-642-40925-7_11.
- [45] H.-M. Park, S.-H. Oh, and S.-Y. Lee, ‘A modified infomax algorithm for blind signal separation’, *Neurocomputing*, vol. 70, no. 1–3, pp. 229–240, Dec. 2006, doi: 10.1016/j.neucom.2006.03.009.
- [46] J. V. Stone, ‘Independent component analysis: an introduction’, *Trends in Cognitive Sciences*, vol. 6, no. 2, pp. 59–64, Feb. 2002, doi: 10.1016/S1364-6613(00)01813-1.
- [47] D. Langlois, S. Chartier, and D. Gosselin, ‘An Introduction to Independent Component Analysis: InfoMax and FastICA algorithms’, *TQMP*, vol. 6, no. 1, pp. 31–38, Mar. 2010, doi: 10.20982/tqmp.06.1.p031.
- [48] A. Hyvärinen and E. Oja, ‘Independent component analysis: algorithms and applications’, *Neural Networks*, vol. 13, no. 4–5, pp. 411–430, Jun. 2000, doi: 10.1016/S0893-6080(00)00026-5.
- [49] T. P. Mutanen, J. Metsomaa, M. Makkonen, G. Varone, L. Marzetti, and R. J. Ilmoniemi, ‘Source-based artifact-rejection techniques for TMS–EEG’, *Journal of Neuroscience Methods*, vol. 382, p. 109693, Dec. 2022, doi: 10.1016/j.jneumeth.2022.109693.
- [50] H. Mäki and R. J. Ilmoniemi, ‘Projecting out muscle artifacts from TMS-evoked EEG’, *NeuroImage*, vol. 54, no. 4, pp. 2706–2710, Feb. 2011, doi: 10.1016/j.neuroimage.2010.11.041.
- [51] M. S. Hämäläinen and R. J. Ilmoniemi, ‘Interpreting magnetic fields of the brain: minimum norm estimates’, *Med. Biol. Eng. Comput.*, vol. 32, no. 1, pp. 35–42, Jan. 1994, doi: 10.1007/BF02512476.
- [52] K. S.-T. Salo, S. M. I. Vaalto, T. P. Mutanen, M. Stenroos, and R. J. Ilmoniemi, ‘Individual Activation Patterns After the Stimulation of Different Motor Areas: A Transcranial Magnetic Stimulation–Electroencephalography Study’, *Brain Connectivity*, vol. 8, no. 7, pp. 420–428, Sep. 2018, doi: 10.1089/brain.2018.0593.

- [53] K. S.-T. Salo, T. P. Mutanen, S. M. I. Vaalto, and R. J. Ilmoniemi, ‘EEG Artifact Removal in TMS Studies of Cortical Speech Areas’, *Brain Topogr*, vol. 33, no. 1, pp. 1–9, Jan. 2020, doi: 10.1007/s10548-019-00724-w.
- [54] M. Mancuso *et al.*, ‘Transcranial Evoked Potentials Can Be Reliably Recorded with Active Electrodes’, *Brain Sciences*, vol. 11, no. 2, p. 145, Jan. 2021, doi: 10.3390/brainsci11020145.
- [55] M. Biabani, A. Fornito, T. P. Mutanen, J. Morrow, and N. C. Rogasch, ‘Characterizing and minimizing the contribution of sensory inputs to TMS-evoked potentials’, *Brain Stimulation*, vol. 12, no. 6, pp. 1537–1552, Nov. 2019, doi: 10.1016/j.brs.2019.07.009.
- [56] L. Fernandez *et al.*, ‘Assessing cerebellar-cortical connectivity using concurrent TMS-EEG: a feasibility study’, *Journal of Neurophysiology*, vol. 125, no. 5, pp. 1768–1787, May 2021, doi: 10.1152/jn.00617.2020.
- [57] J. O. Nieminen *et al.*, ‘Consciousness and cortical responsiveness: a within-state study during non-rapid eye movement sleep’, *Sci Rep*, vol. 6, no. 1, p. 30932, Aug. 2016, doi: 10.1038/srep30932.
- [58] P. Corvo, ‘Analisi della connettività funzionale da segnali EEG in resting state nello spazio sorgente’, Università degli studi di Padova, 2019. [Online]. Available: <https://hdl.handle.net/20.500.12608/24619>
- [59] F. Tadel, S. Baillet, J. C. Mosher, D. Pantazis, and R. M. Leahy, ‘Brainstorm: A User-Friendly Application for MEG/EEG Analysis’, *Computational Intelligence and Neuroscience*, vol. 2011, pp. 1–13, 2011, doi: 10.1155/2011/879716.
- [60] R. M. Gulrajani, *Bioelectricity and biomagnetism*. New York: Wiley, 1998.
- [61] R. Plonsey and D. B. Heppner, ‘Considerations of quasi-stationarity in electrophysiological systems’, *Bulletin of Mathematical Biophysics*, vol. 29, no. 4, pp. 657–664, Dec. 1967, doi: 10.1007/BF02476917.
- [62] H. Hallez *et al.*, ‘Review on solving the forward problem in EEG source analysis’, *J NeuroEngineering Rehabil*, vol. 4, no. 1, p. 46, Dec. 2007, doi: 10.1186/1743-0003-4-46.
- [63] R. Grech *et al.*, ‘Review on solving the inverse problem in EEG source analysis’, *J NeuroEngineering Rehabil*, vol. 5, no. 1, p. 25, Dec. 2008, doi: 10.1186/1743-0003-5-25.
- [64] R. Hyder, N. Kamel, T. B. Tang, and J. Bornot, ‘Brain source localization techniques: Evaluation study using simulated EEG data’, in *2014 IEEE Conference on Biomedical Engineering and Sciences (IECBES)*, Kuala Lumpur, Malaysia: IEEE, Dec. 2014, pp. 942–947. doi: 10.1109/IECBES.2014.7047651.

- [65] S. Casarotto *et al.*, ‘Excitability of the supplementary motor area in Parkinson’s disease depends on subcortical damage’, *Brain Stimulation*, vol. 12, no. 1, pp. 152–160, Jan. 2019, doi: 10.1016/j.brs.2018.10.011.
- [66] I. Winkler, S. Debener, K.-R. Muller, and M. Tangermann, ‘On the influence of high-pass filtering on ICA-based artifact reduction in EEG-ERP’, in *2015 37th Annual International Conference of the IEEE Engineering in Medicine and Biology Society (EMBC)*, Milan: IEEE, Aug. 2015, pp. 4101–4105. doi: 10.1109/EMBC.2015.7319296.
- [67] N. C. Rogasch *et al.*, ‘TESA User Manual’. [Online]. Available: <https://nigelrogasch.gitbook.io/tesa-user-manual/#citations-and-acknowledgements>
- [68] ‘The jamovi project’. 2022. [Online]. Available: <https://www.jamovi.org>
- [69] S. Steegen, F. Tuerlinckx, A. Gelman, and W. Vanpaemel, ‘Increasing Transparency Through a Multiverse Analysis’, *Perspect Psychol Sci*, vol. 11, no. 5, pp. 702–712, Sep. 2016, doi: 10.1177/1745691616658637.